

UNIVERSITY OF CALIFORNIA

Los Angeles

NO TITLE!?!?

A dissertation submitted in partial satisfaction  
of the requirements for the degree  
Doctor of Philosophy in Physics

by

Tyler Christopher Lam

2023

© Copyright by  
Tyler Christopher Lam  
2023

The dissertation of Tyler Christopher Lam is approved.

Michalis Bachtis, Committee Chair

University of California, Los Angeles

2023

## TABLE OF CONTENTS

<b>1</b>	<b>Introduction</b>	<b>1</b>
<b>2</b>	<b>The Standard Model and Searches for Displaced Photons</b>	<b>2</b>
2.1	The Standard Model	2
2.2	Motivations for Long Lived Scalar Bosons	2
<b>3</b>	<b>Experimental Apparatus</b>	<b>3</b>
3.1	The Large Hadron Collider	3
3.1.1	The High Luminosity LHC	6
3.2	The Compact Muon Solenoid	7
3.2.1	CMS Coordinate System	8
3.2.2	Charged Track Momentum Resolution	9
3.2.3	Inner Tracker	10
3.2.4	Electromagnetic Calorimeter	12
3.2.5	Hadronic Calorimeter	14
3.2.6	Muon Detectors	16
3.2.7	Trigger System	21
3.2.8	Event Reconstruction	25
<b>4</b>	<b>Real Time Muon Reconstruction at the Compact Muon Solenoid</b>	<b>29</b>
4.1	Introduction	29
4.2	The Kalman Filter Algorithm	30
4.3	The Kalman Barrel Muon Track Finder	31

4.3.1	Muon Trajectory Propagation . . . . .	32
4.3.2	Covariant Matrices and the Kalman Gain . . . . .	36
4.3.3	Firmware Implementation of the KBMTF . . . . .	38
4.4	Performance of the Kalman Barrel Muon Track Finder . . . . .	39
4.4.1	Trigger Efficiencies and Rate . . . . .	40
4.4.2	Firmware and Emulator Agreement . . . . .	43
4.5	The Phase-2 KBMTF . . . . .	43
<b>5</b>	<b>Search for a Long Lived Scalar Boson . . . . .</b>	<b>47</b>
5.1	Introduction . . . . .	47
5.2	Data and Simulated Samples . . . . .	47
5.2.1	Data Samples . . . . .	47
5.2.2	Simulated Samples . . . . .	48
5.3	Vertex Reconstruction of Displaced Photon Pairs . . . . .	52
5.3.1	Diphoton Kinematics . . . . .	52
5.3.2	Performance of Diphoton Vertex Calculation . . . . .	55
5.4	Event Selection . . . . .	58
5.4.1	Triggers . . . . .	58
5.4.2	Preselection Criteria . . . . .	59
<b>References . . . . .</b>		<b>64</b>

## LIST OF FIGURES

3.15	Designed trigger architecture of the HL-LHC. The addition of the track primitives allows the computation of more advanced reconstruction algorithms at the L1 level [13]. . . . .	24
4.1	The iterative process of propagation and updating a muon track through the KBMTF algorithm. The track properties at the innermost station are stored in order to trigger on muons not originating from the beamline [14] . . . . .	33
4.2	Diagram showing a muon trajectory between two stations with the origin set at the outer station. The x-axis is oriented using the detector vertex and the outer station. . . . .	35
4.3	Calculation of phi propagation coefficients. Units are converted to their digitized form used in firmware calculations. . . . .	36
4.4	$\sigma$ of vertical slice fits of the 2-dimensional histogram in figure 4.3a used to calculate uncertainty coefficients. . . . .	37
4.5	Comparison of efficiency vs cosmic track $d_{xy}$ using cosmic data from the 2018 data taking run. The prompt KBMTF takes the reconstructed $p_T$ using the vertex constrained measurement, while the displaced KBMTF uses the veretx unconstrained measurement. The displaced KBMTF shows substantial improvements to the previous BMTF [15] . . . . .	41
4.6	Rate comparison calculated using 2017 zero bias data of the Phase I BMTF, vertex constrained (prompt) KBMTF, vertex unconstrained (displaced) KBMTF, and displaced KBMTF for displaced tracks. . . . .	42
4.7	Comparison of the track $p_T$ between the firmware and emulator using data from a 2017 Z tag-and-probe sample. hwPt represents the integer value of $p_T$ used in hardware. The emulator and firmware output show 100% agreement across 500000 events. . . . .	44

4.8	Performance of the L1 Barrel Muon algorithms using simulated samples with HL-LHC run conditions. The Track + KBMTF algorithm matches tracks to loose KBMTF muons, while the L1 Track + Muon Stubs algorithm matches tracks to muon stubs. . . . .	46
5.1	Pileup distributions and mean PU from 2011-2023 datataking [1] . . . . .	51
5.2	Geometrical configuration used to reconstruct the displaced vertex of the diphoton pair . . . . .	53
5.3	Geometrical configuration showing the reconstruction of a negative impact parameter . . . . .	55
5.4	Performance of the vertex calculation on signal samples. The fit shows good agreement across all values of generator level $L_{xy}$ and a resolution of $< 3$ cm. . .	56
5.5	The difference between the true and reconstructed vertex grows as the assumed mass departs from the true one. Gen-reconstructed $L_{xy}$ for a $Z + H$ samples under several assumed mass points. . . . .	57
5.6	The $\rho$ for barrel photons and $ z $ for endcap photons for all reconstructed photons using <code>miniAODv2</code> signal samples . . . . .	58

## LIST OF TABLES

4.1	Comparison of FPGA resource utilization [14]. The KBMTF utilizes DSP cores for arithmetic operations to propagate and update tracks and LUTs for the propagation coefficients and approximate Kalman Gain, while the BMTF uses LUTs to assign momentum. . . . .	39
5.1	Table of integrated luminosity per year [16–18]. . . . .	48
5.2	Mass points, lifetimes, and number of simulated $H \rightarrow \Phi\Phi$ events for the $2\gamma 2q$ categories. Number of events generated is halved for the $4\gamma$ categories . . . . .	49
5.3	List of simulated background processes and their cross sections calculated using <code>GenXSecAnalyzer</code> [19] . . . . .	52
5.4	HLT trigger paths used for the Run 2 datasets . . . . .	59
5.5	Cut based ID selection criteria for barrel electrons in Run-2 [20] . . . . .	62
5.6	Cut based ID selection criteria for endcap electrons in Run-2 [20] . . . . .	63

# **CHAPTER 1**

## **Introduction**

## **CHAPTER 2**

# **The Standard Model and Searches for Displaced Photons**

### **2.1 The Standard Model**

### **2.2 Motivations for Long Lived Scalar Bosons**

# CHAPTER 3

## Experimental Apparatus

### 3.1 The Large Hadron Collider

The Large Hadron Collider (LHC) is a circular collider spanning the border between France and Switzerland, based at the European Organization for Nuclear Research (CERN). The central features of the LHC are the superconducting rings, located about 100 m underground with a circumference of 27 km, designed to collide counter-rotating beams of protons or heavy ions at highly relativistic energies. Along the rings lie four major experiments: ATLAS, CMS, ALICE, and LHCb. Both ATLAS and CMS are general purpose detectors, designed to probe a wide range of physics including the Higgs boson, precision measurements of fundamental constants, and physics beyond the standard model (BSM). The remaining two experiments are more specialized; ALICE measures quark gluon plasma produced in heavy ion collisions and LHCb focuses on  $b$ -quark physics and CP violation.

Two prominent aspects of the LHC are the high center of mass energy of the proton beams, referred to using the Mandelstam variable  $\sqrt{s}$ , and high instantaneous luminosity  $\mathcal{L}$ , often referred to as just luminosity. High  $\sqrt{s}$  allows for the production of more massive particles, giving more access to possible BSM physics, while high luminosity is essential for measuring rare processes and precision measurements. A process with cross section  $\sigma$  will have a rate  $R$  given by

$$R = \mathcal{L}\sigma \tag{3.1}$$

The cross section  $\sigma$  is a measure of how probable a process is to occur, and is measured in

units of area. A frequent used unit for cross sections is a barn (b), corresponding to  $100 \text{ fm}^2$ . Conversely, luminosity uses units of  $\text{Hz}/\text{b}$ . In cases where the relevant quantity is the total number of events, the integrated luminosity can be defined as  $\mathcal{L}_{\text{int}} = \int \mathcal{L} dt$  to give

$$N_{\text{events}} = \mathcal{L}_{\text{int}} \sigma \quad (3.2)$$

The luminosity depends on the characteristics of the proton beam and can be written in terms of the operational parameters of the detector given by

$$\mathcal{L} = \frac{N_b^2 n_b f_{\text{rev}} \gamma_r}{4\pi \epsilon_n \beta^*} F \quad (3.3)$$

where  $N_b$  is the number of particles per bunch,  $n_b$  is the number of bunches per ring,  $f_{\text{rev}}$  is the LHC revolution frequency,  $\gamma_r$  is the Lorentz factor for the proton,  $\epsilon_n$  is the transverse normalized beam emittance,  $\beta^*$  is the amplitude function at the collision point, and  $F$  is a geometric reduction factor based on the crossing angle of the two beams. The nominal design parameters of the LHC were intended to support a peak luminosity of  $12 \text{ Hz/nb}$  [21], but were exceeded by nearly twice that value of  $20.7 \text{ Hz/nb}$  during 2017 data taking and again with  $21.4 \text{ Hz/nb}$  in 2018. The LHC produced an integrated luminosity of  $41.6 \text{ fb}^{-1}$  in 2016,  $49.8 \text{ fb}^{-1}$  in 2017, and  $67.9 \text{ fb}^{-1}$  in 2018 for a total of  $164 \text{ fb}^{-1}$  during run 2 data taking. A more detailed breakdown of the LHC luminosity records can be seen in Fig. 3.1.

The protons used in collisions are extracted from hydrogen atoms by using ionizing electric fields to strip them of their electrons. Protons are first accelerated to an energy of  $50 \text{ MeV}$  through a linear accelerator Linac2 before entering the Proton Synchrotron Booster (PSB), where they reach a kinetic energy of  $1.4 \text{ GeV}$ . Next, the protons are accelerated by the Proton Synchrotron (PS) and Super Proton Synchrotron (SPS), where they are accelerated to  $26 \text{ GeV}$  and  $450 \text{ GeV}$  respectively. Finally, the beams are injected into the LHC where they undergo acceleration to  $6.5 \text{ TeV}$ , producing the desired center of mass energy of  $\sqrt{s} = 13 \text{ TeV}$ .

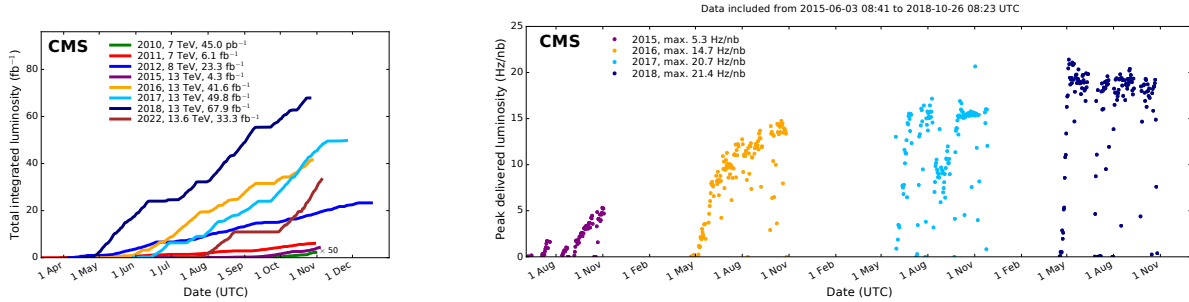


Figure 3.1: LHC luminosity report. Left: breakdown of the CMS integrated luminosity by year from 2010-2022. Right: peak instantaneous luminosity from 2016-2018 data taking [1].

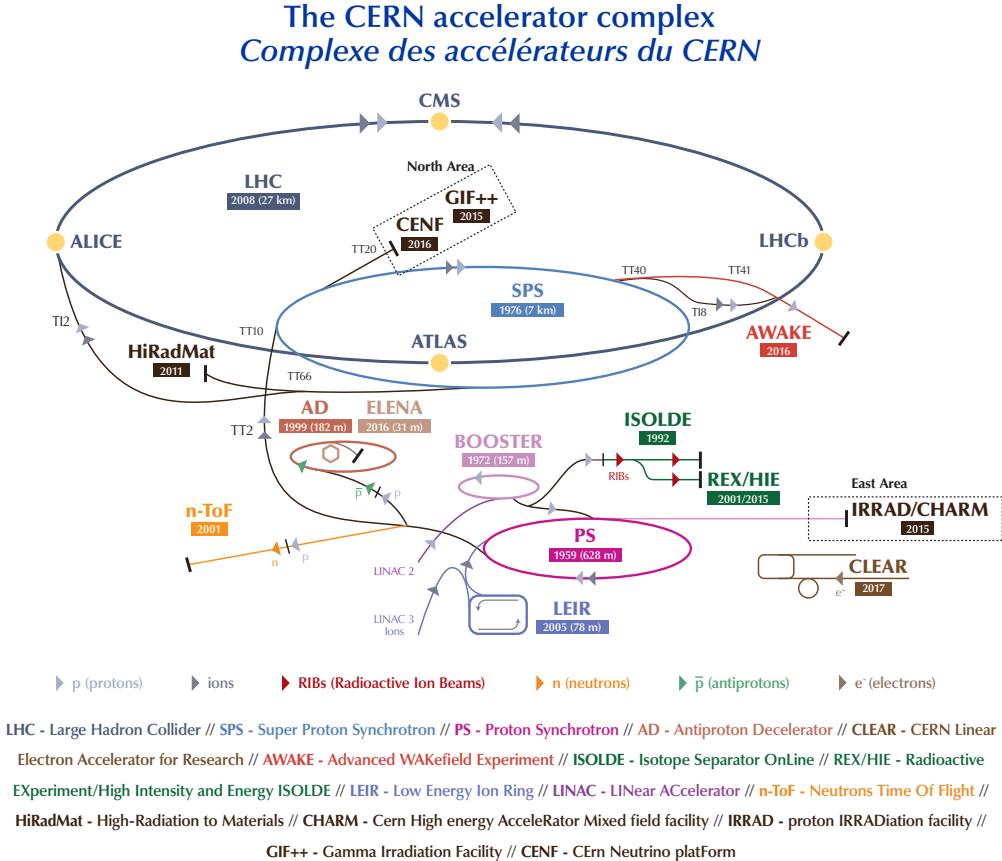


Figure 3.2: Diagram of the CERN accelerator complex during 2018 data taking [22]. Protons begin as hydrogen atoms at Linac2 and are accelerated in several stages to reach 6.5 TeV.

### 3.1.1 The High Luminosity LHC

The LHC is designed to go through periods of near continuous data taking, followed by long shut downs during which the detectors undergo various upgrades. As of the time of this writing, the LHC is currently in its third data taking run (Run 3), which is planned to operate from 2022-2025. The end of Run 3 marks the end of Phase-1 and the start of the third long shutdown (LS3), during which the LHC will receive major upgrades to increase the peak instantaneous luminosity up to 75 Hz/nb [14], over six times the designed peak luminosity and three times the peak luminosity achieved as of Run 2. The upgraded high luminosity LHC (HL-LHC) will gather substantially more data, which better allows experiments to probe rare processes and measure precise values predicted from the standard model.



Figure 3.3: Timeline of runs and shutdowns leading to the HL-LHC, showing the improvements to  $\sqrt{s}$  and  $\mathcal{L}$  [2]. The extended year-end technical stops (EYETS) are shorter shutdowns generally for routine maintenance, although upgrades such as the CMS Pixel Detector upgrade can occur during this time as well.

## 3.2 The Compact Muon Solenoid

The Compact Muon Solenoid (CMS) is one of the two general purpose detectors at the LHC, designed to reconstruct physics events from proton-proton collisions. It is a cylindrical apparatus with its major axis aligned with the proton beams from the LHC, consisting of several concentric layers of specialized detectors. The innermost layer consists of a silicon tracker, followed by an electromagnetic and hadronic calorimeter (ECAL and HCAL, respectively). Surrounding those is the superconducting solenoid, which provides a 3.8 T magnetic field to the trajectory of charged particles. Lastly, layers of muon chambers are interspersed with an iron return yolk, designed to contain the magnetic field lines near the muon chambers.

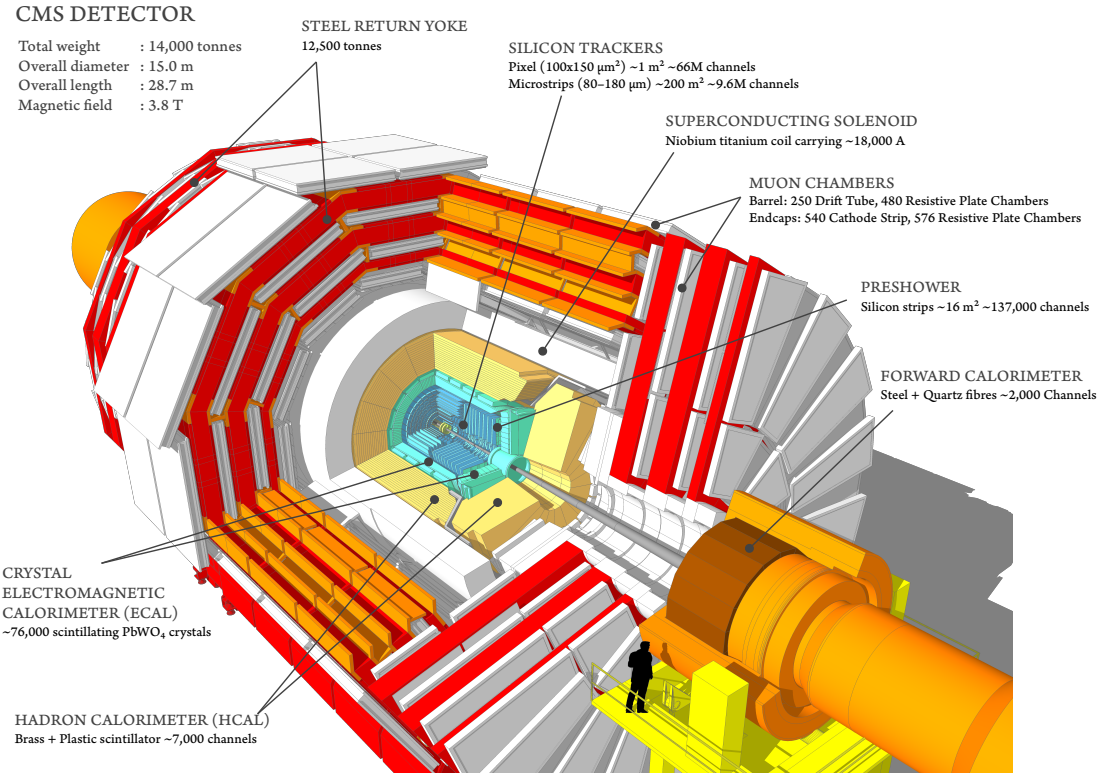


Figure 3.4: Cutaway diagram of CMS showcasing major detector components [3].

### 3.2.1 CMS Coordinate System

The origin of the CMS coordinate system is located at the center of the detector, at the nominal collision point of the proton beams. The  $+\hat{x}$  axis points radially towards the center of the LHC, while the  $+\hat{y}$  axis points vertically upward. This sets the  $+\hat{z}$  direction along the beamline, counterclockwise along the LHC. Due to the cylindrical symmetry of CMS, coordinates in the transverse  $\hat{x}\text{-}\hat{y}$  plane are commonly replaced with the radius  $r$  and the azimuthal angle  $\phi$ , which is measured from the positive  $\hat{x}$ -axis. The polar angle  $\theta$  is measured from the  $+\hat{z}$ -axis, though in practice this variable is rarely used. It is more common to define the polar angle in terms of the pseudorapidity  $\eta$ , which is defined as

$$\eta = \frac{1}{2} \ln \left( \frac{|\mathbf{p}| + p_z}{|\mathbf{p}| - p_z} \right) = -\ln \tan \left( \frac{\theta}{2} \right) \quad (3.4)$$

The motivation for using  $\eta$  instead of  $\theta$  stems from a fundamental property of hadron colliders: the center of mass frame for particle production rarely coincides with the lab frame. Thus, when measuring the separation between particles, it is useful to define quantities that remain invariant under Lorentz transformations in the  $\hat{z}$  direction. The rapidity  $y$  (not to be confused with the Cartesian coordinate  $\hat{y}$ ) is defined as

$$y = \frac{1}{2} \ln \left( \frac{E + p_z}{E - p_z} \right) \quad (3.5)$$

It is trivial to show that differences in  $y$  remain invariant under Lorentz boosts along the  $\hat{z}$ -axis. In the highly relativistic limit, which is valid for most particles produced at the LHC, rapidity approaches pseudorapidity as  $E \approx |\mathbf{p}|$ . The angular separation between two particles can then be expressed as an invariant quantity under Lorentz boosts as  $\Delta R = \sqrt{(\Delta\phi)^2 + (\Delta\eta)^2}$ . One advantage of pseudorapidity is that  $\eta$  can be calculated using only geometric quantities of the detector, whereas  $y$  requires calculating both the energy and momenta of a particle, making pseudorapidity the natural choice for defining the polar

angle.  $\eta$  can range from  $(-\infty, \infty)$ , where  $\eta = \pm\infty$  points directly along the  $\pm\hat{z}$  axis. Higher values of  $|\eta|$  are commonly referred to as "forward".

### 3.2.2 Charged Track Momentum Resolution

The 3.8 T magnet curves the trajectory of charged particles, which allows us to precisely determine their momentum. Using the geometry described in section 3.2.1, a particle with charge  $q$  and transverse momentum  $p_T$  travels in a circular trajectory with radius  $R$  when viewed in the  $r\text{-}\phi$  plane. Per the Lorentz Force Law, these can be related by  $p_T = qBR$ . In particle physics, when working with an object of elementary charge, this is commonly rewritten as

$$p_T = 0.3BR \text{ [GeV/c]} \quad (3.6)$$

The track followed by a charged particle traveling over a length  $L$  can be described by the sagitta  $s$  shown in figure 3.5, defined by

$$s = R - \sqrt{R^2 - \frac{L^2}{4}} \quad (3.7)$$

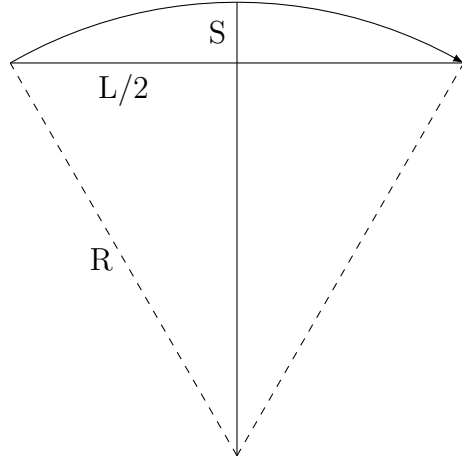


Figure 3.5: Diagram showing the sagitta for a charged particle track

For highly energetic particles, the length  $L$  is substantially smaller than the radius  $R$ , so

the sagitta can be approximated as

$$s \approx \frac{L^2}{8R} = \frac{0.3BL^2}{8p_T} \quad (3.8)$$

The relative uncertainty of the momentum is proportional to the uncertainty of the sagitta, the track length L, and the magnetic field B as

$$\frac{\delta p_T}{p_T} \propto \frac{p_T}{BL^2} \delta_s \quad (3.9)$$

The uncertainty on the sagitta  $\delta s$  is analogous to the hit resolution of a given detector. Therefore, a long lever arm and high magnetic field strength are crucial to precisely determine the momentum of energetic particles.

### 3.2.3 Inner Tracker

The CMS inner tracker is the first detector surrounding the primary interaction point (IP). Its purpose is to measure the tracks from charged particles as they curve in the strong magnetic field within CMS in order to calculate their momentum and reconstruct secondary vertices. As the closest detector to the primary IP, the tracker experiences the highest particle flux within CMS, and must have high enough granularity to distinguish the multitude of tracks. This high granularity also lends the inner tracker the best momentum resolution for charged tracks out of all the subdetectors comprising CMS, with a momentum resolution of 2.8% for a 100 GeV muon [23]. The high flux also makes the detector susceptible to radiation damage, so the tracker must be robust in order to maintain efficiency over the long operational period of the LHC.

The inner tracker utilizes silicon tracking modules composed of P-N type junctions to detect the location of charged particles. When an external voltage is applied to a module, particles passing through will deposit energy and create electron-hole pairs, which drift to

their respective electrodes and generate an electrical signal. The applied voltage is tuned such that only a small amount of energy is required to produce electron-hole pairs, which reduces the total amount of material required in order to minimize the energy loss of the charged particles. The inner layer of the tracker is composed of higher granularity pixel detectors, while the outer layer is composed of coarser silicon strips.

### 3.2.3.1 Silicon Pixel Detector

The pixel detector is comprised of 124 million silicon pixel sensors, each with an area of  $100 \times 150 \mu\text{m}^2$  and a thickness of 300  $\mu\text{m}$ . The barrel (BPIX) consists of four cylindrical layers of pixel sensors spanning from  $z = -54 \text{ cm}$  to  $z = 54 \text{ cm}$  at radii of  $r = 2.9, 6.8, 10.9,$  and 16 cm. The endcap (FPIX) consists of three layers located at  $z = \pm 29.1, \pm 39.6,$  and  $\pm 51.6 \text{ cm}$ , which when combined with the barrel nets a total sensitive area of  $1.85 \text{ m}^2$  with coverage up to  $|\eta| < 2.5$ . With regards to detector performance, the pixel detector provides spatial resolution of  $9.5 \mu\text{m}$  in the  $r\text{-}\phi$  direction and  $22.2 \mu\text{m}$  in the  $z$  direction, as well as a hit efficiency of  $> 99\%$  in each layer at nominal LHC luminosity, with the innermost BPIX layer dropping to 97.5% at peak run 2 efficiency [4].

### 3.2.3.2 Silicon Strip Detector

The silicon strip detector surrounds the pixel detector, and is segmented into a tracker inner barrel (TIB), tracker outer barrel (TOB), tracker inner disks (TID), and tracker endcap (TEC). The TIB consists of four layers covering  $|z| < 65 \text{ cm}$  and radius  $25.5 \text{ cm} < r < 49.8 \text{ cm}$ . The endcaps of the TIB are covered by the TID, consisting of three disks covering  $90 < |z| < 90 \text{ cm}$ . Surrounding the TIB is the TOB, with six layers spanning  $|z| < 188 \text{ cm}$  and  $60.8 < |r| < 108 \text{ cm}$ . Lastly, both the TOB and TID are closed by the TEC, which covers radii ranging from  $22 < r < 113.5 \text{ cm}$  and stretches from  $124 < |z| < 280 \text{ cm}$ .

The strip detector modules function similarly to the pixel modules, but utilize much

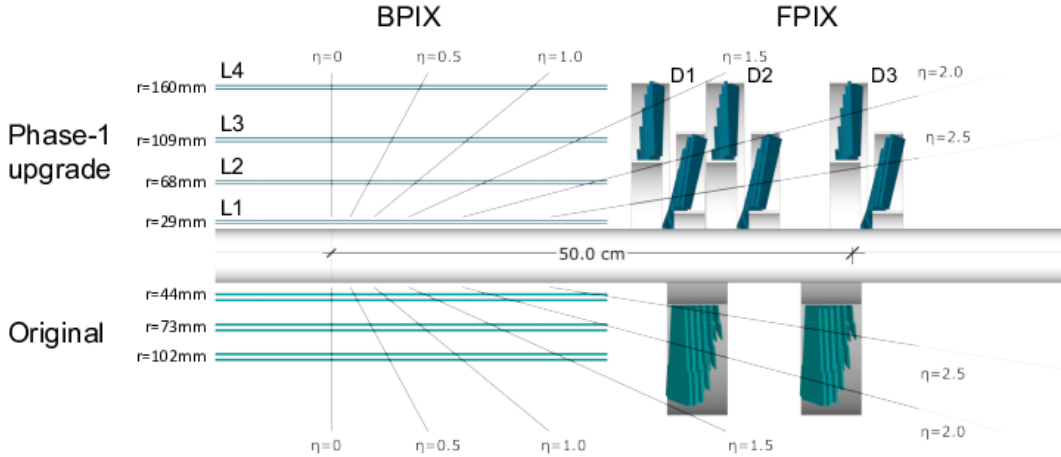


Figure 3.6:  $r$ - $z$  slice of the CMS pixel detector comparing original design (bottom, teal) with the Phase-I upgrade implemented in 2016/17, which added one layer to both the FPIX and BPIX (top, blue) [4].

larger silicon strips due to the expected reduced particle flux compared to the pixel detector. Each strip detector is composed of  $300\ \mu\text{m}$  thick micro-strip sensors with pitch varying from  $80 - 205\ \mu\text{m}$  to form  $7 - 12.5\ \text{cm}$  long strip modules. Overall, the strip detector uses 15,148 modules covering an area of  $200\ \text{m}^2$  up to  $|\eta| < 2.5$ .

### 3.2.4 Electromagnetic Calorimeter

The CMS Electromagnetic Calorimeter (ECAL) is designed to stop and capture the energy of photons and electrons. When a high energy photon or electron enters the ECAL, it primarily interacts with the material in the detector through  $e^+e^-$  pair production or bremsstrahlung, respectively. These processes create more photons and electrons that result in an electromagnetic cascade until the particles lose enough energy that ionization and compton scattering processes begin to dominate. This process is known as an electromagnetic shower. The light from these showers is measured using photodetectors to determine the initial energy of the incident particle with resolution given by

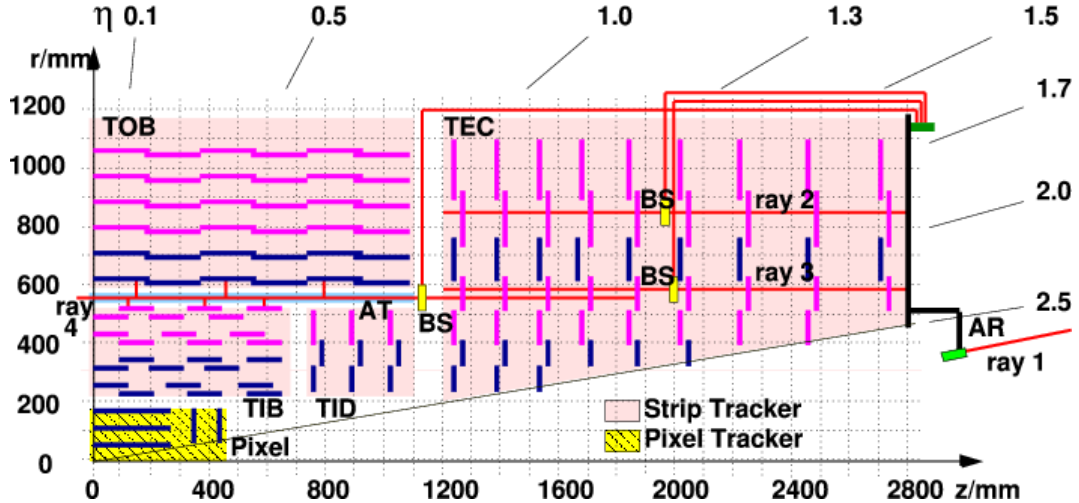


Figure 3.7:  $r$ - $z$  slice of the CMS silicon detector, detailing the four main components (TIB, TOB, TID, and TEC) of the strip detector. Pixel detector is shown in its Run-I configuration [5].

$$\left(\frac{\sigma_E}{E}\right)^2 = \left(\frac{2.8\%}{\sqrt{E/\text{GeV}}}\right)^2 + \left(\frac{12\%}{E/\text{GeV}}\right)^2 + (0.3\%)^2 \quad (3.10)$$

The first term arises from statistical fluctuations in the electromagnetic shower and light production, which is a poisson process and therefore proportional to  $1/\sqrt{E}$ . The second term is due to the noise in the detector electronics. The last constant term is due to imperfections in the detector such as non-uniformity, radiation damage, and calibration uncertainty. The material used for an electromagnetic calorimeter can be characterized by the radiation length ( $X_0$ ) and molière radius ( $R_M$ ). The radiation length is the average distance an electron will travel before its energy is reduced by a factor of  $1/e$ , and is roughly proportional to  $A/Z^2$ , where  $A$  is the atomic mass and  $Z$  is the atomic number. The molière radius is directly proportional to the radiation length and measures the spread of an electromagnetic shower in the transverse direction. Both are generally measured in units of  $[\text{g cm}^{-2}]$ , but can be divided by the density of the material to obtain a distance in  $[\text{cm}]$ . A low radiation length and Molière radius ensure all of the energy is captured in the detector and is contained to a

small area to precisely determine the position of an incident particle. It is for this reason that the ECAL is composed of lead-tungstate ( $\text{PbWO}_4$ ): a dense, high Z scintillator crystal with  $X_0 = 7.39 \text{ g/cm}^2$  (or  $0.89 \text{ cm}$  after dividing by the density of  $\text{PbWO}_4$ ) and  $R_M = 2.2 \text{ cm}$  [24].

The ECAL is constructed from  $61200 + 15000$  lead-tungstate crystals in the barrel + endcap region. Barrel crystals have a cross sectional area of  $2.2 \times 2.2 \text{ cm}^2$  to match the molière radius and a depth of  $23 \text{ cm}$  (or  $25.8 X_0$ ), and are arranged in rings along the  $\phi$  direction, tilted to align with lines of constant  $\eta$ . The barrel has an inner radius of  $129 \text{ cm}$  and covers an eta region up to  $|\eta| < 1.479$ . Endcap crystals have a slightly higher cross sectional area of  $2.6 \times 2.6 \text{ cm}^2$  and a slightly lower depth of  $22 \text{ cm}$ , and are arranged in an  $x$ - $y$  grid. The endcap provides the remaining coverage from  $1.479 < |\eta| < 3.0$ . A diagram showing the geometry of the ECAL can be seen in figure 3.8. The size and alignment of the crystals is designed to contain showers from incident photons/electrons within a  $2 \times 2$  grid of crystals.

One common process in CMS is the production of  $\pi^0$ s, which decay to two photons. When the two photons deposit their energy into the ECAL, they can fake a signal from a single high energy photon. In order to identify these background events, a higher granularity detector known as a preshower is placed before the ECAL endcap. It consists of a layer of lead absorber to initiate the shower, followed by silicon strip sensors to measure the tracks within the shower. The lead has a thickness of  $1.57 \text{ cm}$  (or  $2.8X_0$ ), which is thick enough to reliably cause a shower while only causing energy loss of a few percent before the shower can reach the ECAL. The silicon strips are similar to those in the inner tracker, with a pitch of  $1.9 \text{ mm}$  [25].

### 3.2.5 Hadronic Calorimeter

The CMS Hadronic Calorimeter (HCAL) is a sampling calorimeter surrounding the ECAL. Unlike the ECAL, which is a homogeneous calorimeter where the crystals both induce showers and scintillate, the HCAL is composed of alternating layers of dense absorber and scintilla-

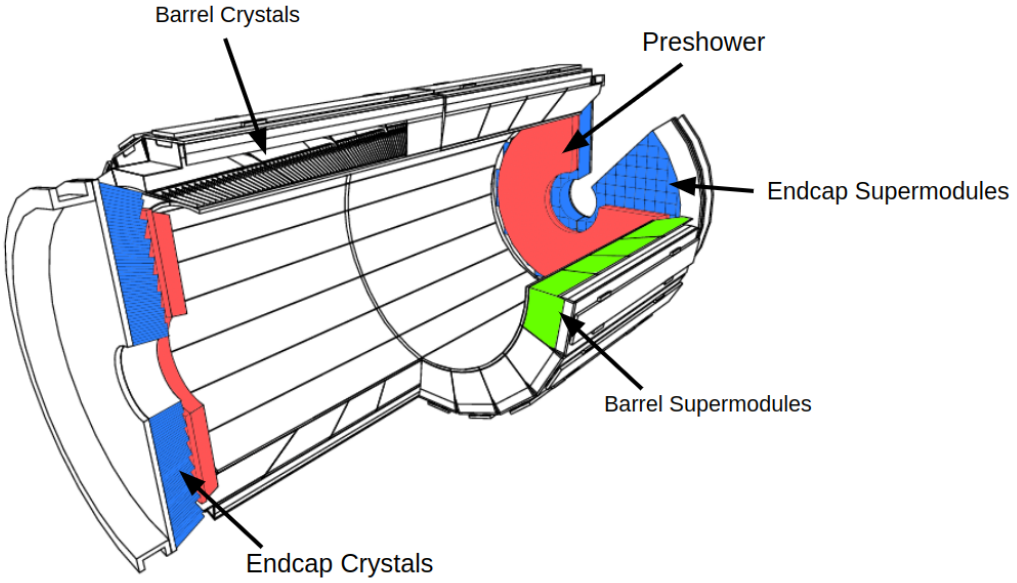


Figure 3.8: Geometry of the CMS ECAL showing the barrel, endcap, and preshower, adapted from [6].

tor. The absorber induces hadronic showers - cascades of hadrons resulting from inelastic scattering off a target nuclei. Particles in hadronic showers then pass through the scintillator, which produces light that gets transmitted through wavelength shifting fibers and read out by photodetectors, before repeating this process with the next layer of absorber/scintillator. The measured energy can be summed in sequential layers of detectors (referred to as "towers") to calculate the total energy of the incident hadron. As an additional complication, several hadrons decay to electrons or photons, which will create electromagnetic showers, requiring the scintillator to have good response to electromagnetic interactions. The HCAL must be hermetic, as a complete picture of the energy from proton collisions is required to infer the production of particles like neutrinos, which are otherwise invisible to the detector.

The relevant property for a hadronic absorber is the nuclear interaction length  $\lambda_I$ , which is the mean distance a hadron will travel before undergoing an inelastic nuclear interaction. Like the radiation length,  $\lambda_I$  is measured in  $[g\text{ cm}^{-2}]$  and can be divided by the density to

obtain a distance in [cm]. It is proportional to the density of nuclear matter, which goes as  $A^{1/3}$ . The HCAL uses a combination of brass and stainless steel, which have an interaction length of  $\sim 16.5$  cm [26].

The HCAL consists of four subsystems: an inner barrel (HB), an outer barrel (HO), an endcap (HE), and a forward calorimeter (HF). The HB covers  $|\eta| < 1.3$  with 36 azimuthal wedges, each containing 17 layers of alternating brass absorber and scintillator. These wedges begin at a radius of 1.806 m and are 89 cm thick, resulting in a minimum of  $5.3 \lambda_I$  at  $\eta = 0$ , increasing to  $10 \lambda_I$  and  $\eta = 1.2$ . The HE consists of two disks, also formed of 36 wedges with 19 layers of brass absorber and scintillator, totaling  $10 \lambda_I$  in order to contain highly boosted, forward showers resulting from quarks and gluons.. The HE extends the coverage of the HCAL up to  $|\eta| < 3.0$ . The HO is located outside the magnetic coil to catch high energy ( $> 100$  GeV) hadrons that escape the HB. It consists of five rings in eta, covering up to  $|\eta| < 1.2$ , and relies on the iron solenoid to induce hadronic showers. The HF covers the most forward region of  $3 < |\eta| < 5$ . This zone has the highest exposure of radiation, and so the detector must be sensitive only to the highest energy particles and robust against damage from heavy radiation. It uses steel as the absorber and quartz fibers to scintillate through Cherenkov radiation. The four subsystems provides a minimum of  $10 \lambda$  to capture incident hadrons.

### 3.2.6 Muon Detectors

The muon chambers lie outside the magnetic solenoid as the outermost subsystem in CMS. Due to the distance and amount of material between them and the primary IP, they are the lowest occupancy detectors, with few particles other than muons able to reach them before decaying or stopping in the inner subsystems. Although they lie outside the solenoid, the iron yolk pulls the magnetic field back to curve the trajectory of muons, which is required calculate their momenta. The detector subsystem is composed of three types of gaseous detection chambers: drift tubes (DTs), resistive plate chambers (RPCs), and cathode strip

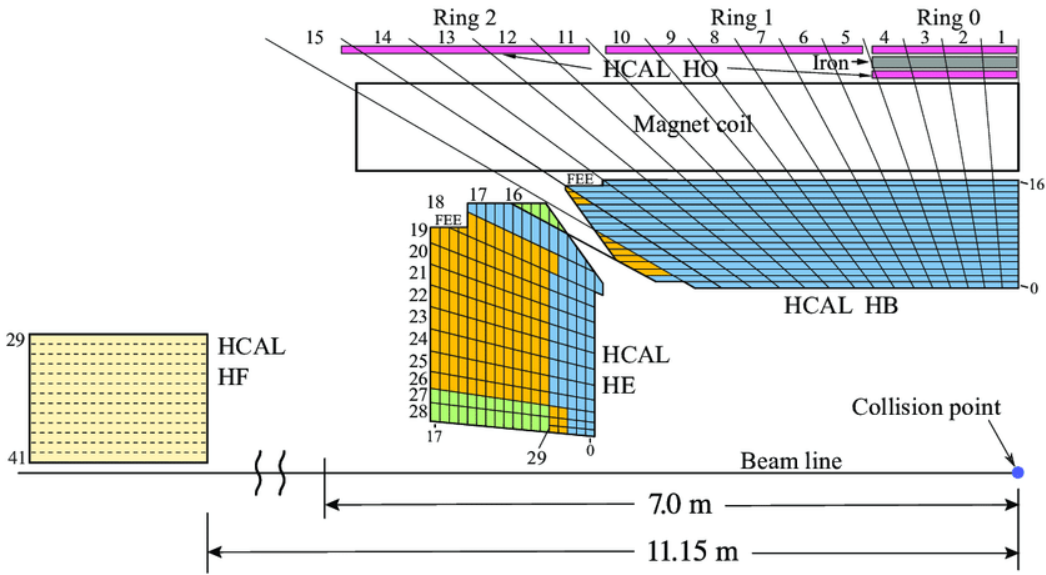


Figure 3.9:  $r$ - $z$  slice of the CMS HCAL showing the HB, HE, HF, and HO [7].

chambers (CSCs). A diagram showing the configuration of these detection chambers can be seen in figure 3.10.

The operating physics principles of all three chambers are similar: muons pass through a gas mixture and ionize the gas, knocking loose electrons. Anodes and cathodes create an electric field inside the gas chamber, causing the electrons to drift to the anode where they can be measured and read out by electronics. Electrons that are excited but not ionized from the incident muon will emit photons as they transition back to a lower energy level, thus a quenching gas is used to absorb these photons to prevent further cascades. The specifics of the three detectors are described in sections 3.2.6.1-3.2.6.3.

### 3.2.6.1 Drift Tubes

Drift tubes are used in the barrel of the muon system, covering  $|\eta| < 1.2$ . They consist of long chambers filled with an mixture of Ar/CO<sub>2</sub>, with an anode wire running lengthwise through the center and cathode strips along the edges. Electrode strips along the outer edge of the chamber shape the electric field lines to linearize the drift velocity of electrons

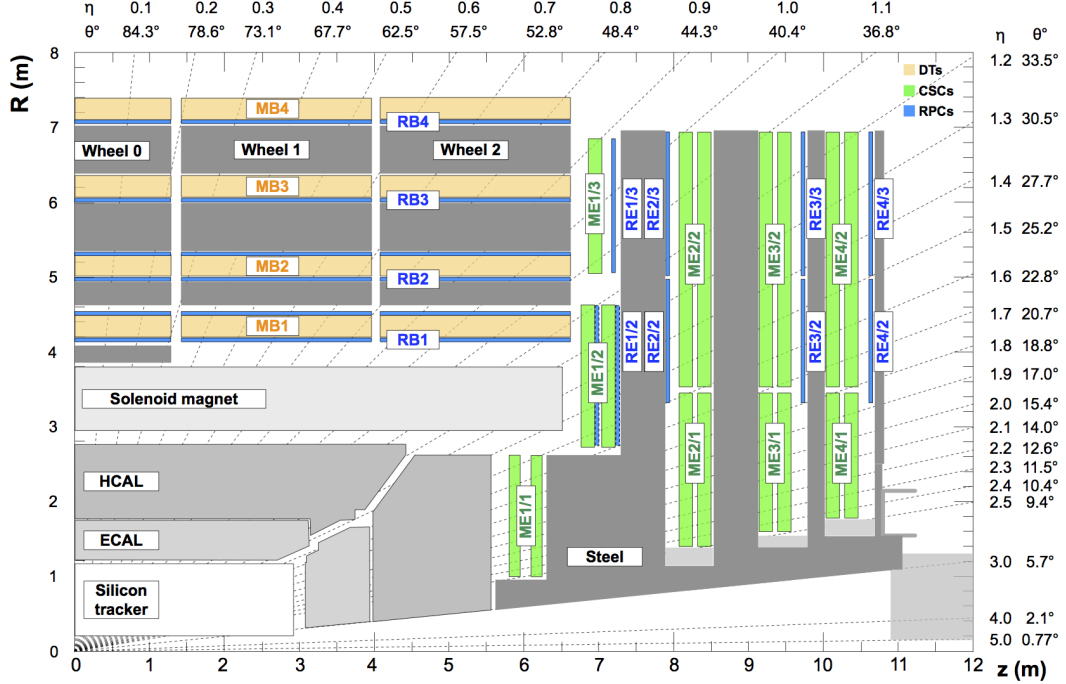


Figure 3.10:  $r$ - $z$  cross section of the CMS muon detector subsystem, configured for the 2016–2018 data taking run. The barrel consists of five wheels of DTs and RPCs in  $\eta$ , each wheel consisting of four layers in  $r$  and 12 sectors in  $\phi$ , covering up to  $|\eta| < 1.2$ . The endcap consists of four layers of DTs and RPCs in  $z$  [8].

throughout the chamber. When a muon passes through the chamber, ionized electrons follow the electric field lines towards the anode wire. Due to the known field inside the chamber, the drift time can be used to calculate the transverse distance from the wire to the incident muon with a resolution of  $250 \mu\text{m}$ . The DTs are arranged in superlayers, which consist of 4 layers of DTs, with subsequent superlayers alternating in the  $r$ - $z$  and  $r$ - $\phi$  direction in order to obtain the muon trajectory/curvature in both the  $\eta$  and  $\phi$  direction. Figure 3.11 shows a diagram of a DT superlayer and a single DT cell.

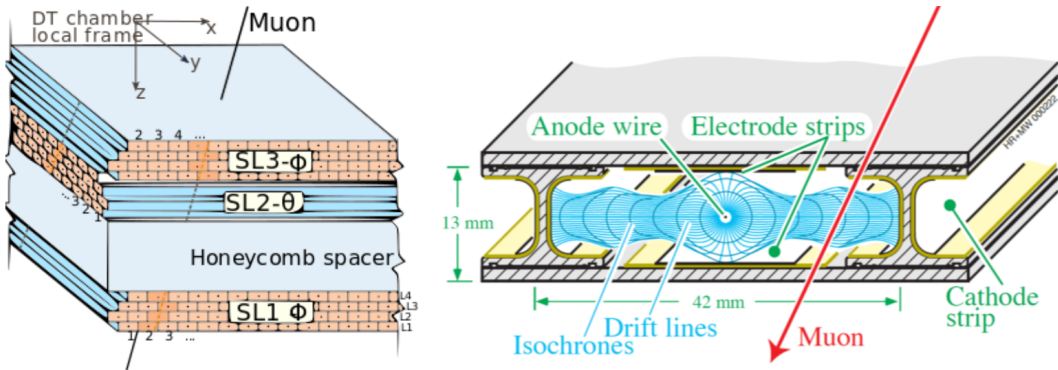


Figure 3.11: Drift tube superlayers are aligned in alternating orientations in order to provide a complete picture of muon trajectories (left). A cross section of a single drift tube chamber (right). Electrons ionized from the muon drift to the anode wire to produce a measurable current [9].

### 3.2.6.2 Cathode Strip Chambers

Cathode strip chambers are used in the endcaps of the muon system to provide coverage from  $0.9 < |\eta| < 2.4$ . CSC modules are trapezoidal chambers filled with a mixture of Ar/CO<sub>2</sub>/CF<sub>4</sub> and arranged in disks to cover the muon endcap. Each module is composed of six layers of radial cathode strips, which have high granularity in  $\phi$ , and transverse anode wires which provide granularity in  $r$ . Similar to the DTs, muons passing through CSC chambers ionize the gas molecules, knocking loose electrons which drift to the anode wires. The charge from these electrons can be measured and provides the position of the muon in  $r$ . Simultaneously,

the electrons induce a charge in the cathode strips, which provides the position of the muon in  $\phi$ . One chamber provides a spatial resolution of between  $40 - 50 \mu\text{m}$  with a time resolution of 3 ns.

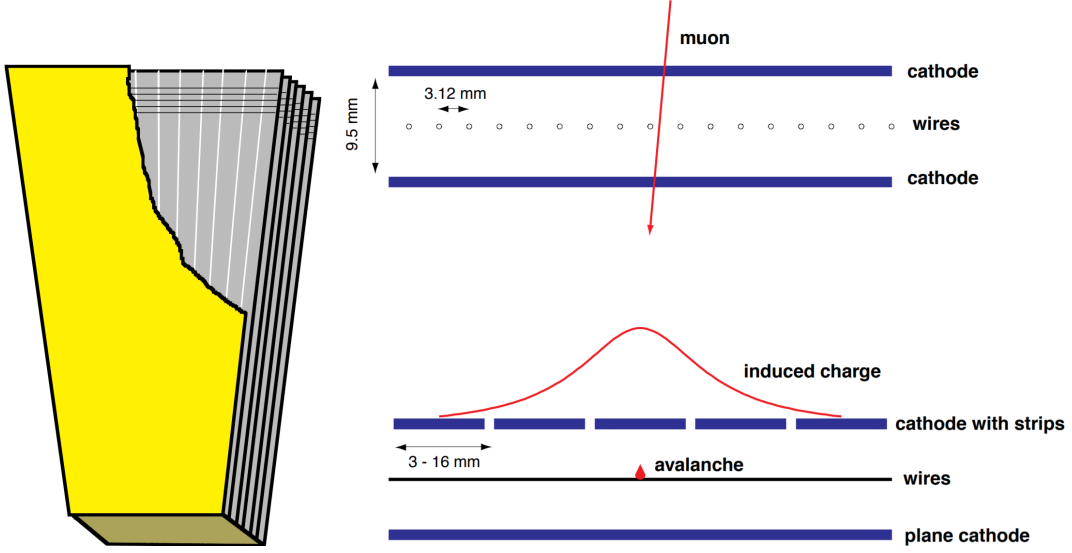


Figure 3.12: Cut-away diagram of a single CSC module showing the six layers of radial cathode strips and transverse anode wires (left). Muons ionize the gas chamber, causing an avalanche of electrons on the anode wires and inducing a charge on the cathode strips (right) [10].

### 3.2.6.3 Resistive Plate Chambers

RPC detectors are used in conjunction with the DTs and CSCs in both the barrel and endcap. One RPC consists of two high resistivity plastic plates: one positively charged anode and a negatively charged cathode which create a strong, uniform electric field between the two. The space between the two plates is filled with a mixture of 95%  $\text{C}_2\text{H}_2\text{F}_4$  and 5% iso- $\text{C}_4\text{H}_{10}$ . Incident muons ionize the gas between the two plates, which cause a cascade of electrons towards the anode plate due to the strong electric field. External metal strips lie outside the anode in order to measure the avalanche of electrons. The coarse nature of the strips means the RPC spatial resolution is lower than that of the CSCs and DTs at around

1 cm, but the time resolution is much faster on the order of 1 ns. For this reason they are used to supplement the CSC and DTs to aid with triggering and accurate timing.

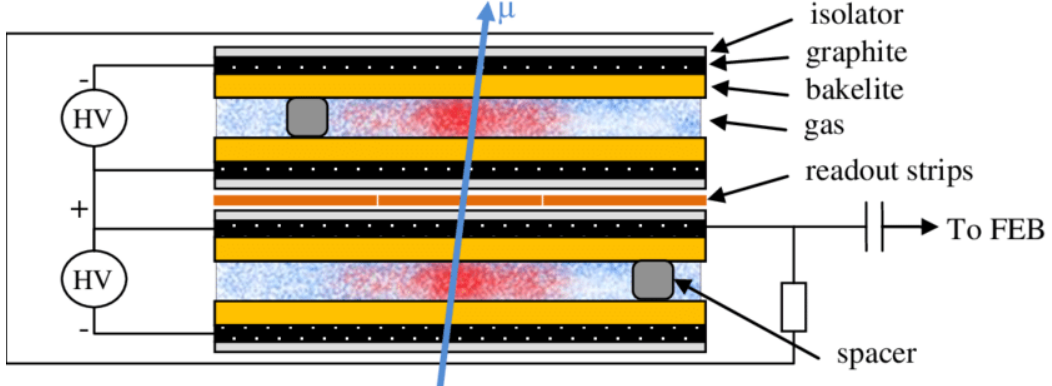


Figure 3.13: Diagram of the double RPC at CMS. Incident muons ionize the gas, causing a cascade of electrons towards the readout strips [11].

### 3.2.7 Trigger System

The high luminosity of the LHC yields an incredibly high rate of information to store from the various detectors. Each event contains approximately 1 MB of data to store, which would take bandwidth and storage space beyond current capacities to save given the 40 MHz collision rate. Additionally, many events are soft collisions that do not contain interesting physics worth storing for further analysis. In order to reduce the rate of events and select only the most interesting collisions, CMS employs a two level trigger system. The first level is known as the Level-1 (L1) trigger and uses hardware to identify physics objects in real time. The second is known as the High-Level trigger (HLT), consisting of a conventional CPU farm which performs more advanced calculations.

### 3.2.7.1 Level-1 Trigger

The L1 trigger utilizes special processors such as Field Programmable Gate Arrays (FPGAs) in order to process coarse information from the calorimeters and muon chambers in real time. The coarse detector information, known as trigger primitives, is subjected to several algorithms to create physics objects (e.g. muons, electrons/photons, etc). Objects passing a predetermined set of criteria are called trigger "seeds", with events that satisfy at least one seed getting passed to the HLT. A diagram of the L1 trigger architecture can be seen in figure 3.14. This entire decision making process must take place in  $3.2 \mu\text{s}$  after a bunch crossing. As this is greater than the time between bunch crossings, the L1 trigger must be pipelined in order to operate continuously, while the full data is kept in a rolling buffer and read out only if the event passes a trigger seed. The L1 trigger was designed to accept events at a maximum rate of about 100 kHz, meaning only one in every four hundred events is passed to the HLT.

The L1 trigger will undergo several changes during LS3 as a result of the HL-LHC upgrade discussed in section 3.1.1. The main consequence of higher luminosity is an increase in additional proton collisions along the beamline per bunch crossing, known as pileup. Interesting physics events generally stem from a single hard scattering interaction, known as the primary vertex (PV), with lower energy pileup collisions creating background that can obscure the physics from the PV. The L1 trigger is well equipped for the average 40 pileup for Run 3, but will require upgrades in order to accommodate the expected 200 pileup for the HL-LHC. As part of the L1 trigger update, the maximum bandwidth will be increased from 100 kHz to 750 kHz and the trigger decision latency will be increased from  $3.2 \mu\text{s}$  to  $12.5 \mu\text{s}$ . Additionally, new tracker primitives will be available as inputs to the calorimeters and muon triggers. These primitives allow the precise  $p_T$ ,  $\eta$ , and  $\phi$  information from tracks to be associated with calorimeter clusters and muon primitives, greatly increasing the precision and efficiency of L1 reconstruction. The proposed trigger architecture for the HL-LHC can be seen in figure 3.15.

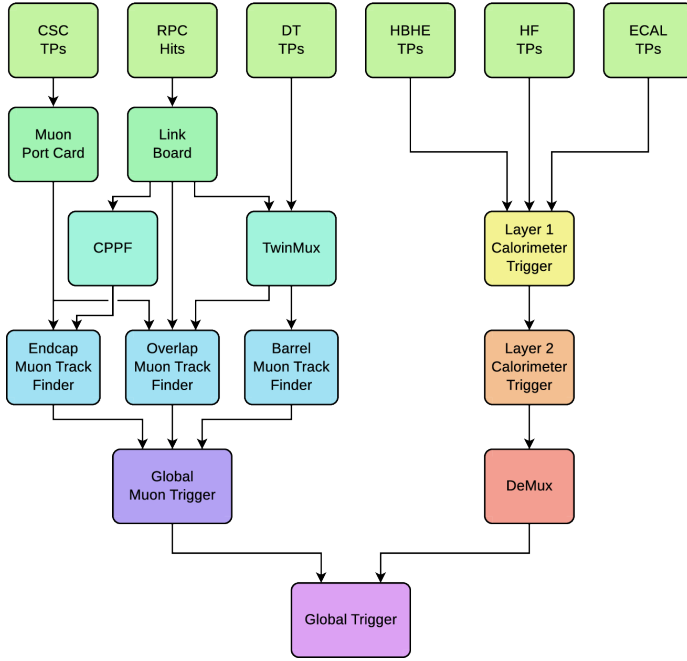


Figure 3.14: Block diagram of the CMS Level-1 Trigger architecture during Run 2 [12]. Muon objects found in the barrel, overlap, and endcap regions are ranked and sorted using their momentum and quality criteria before being passed to the Global Muon Trigger (GMT), which cleans duplicate tracks and selects the top eight muons. The muons are then passed to the global trigger, which combines the muons with objects created from the calorimeters and makes the final decision to pass the event to the HLT.

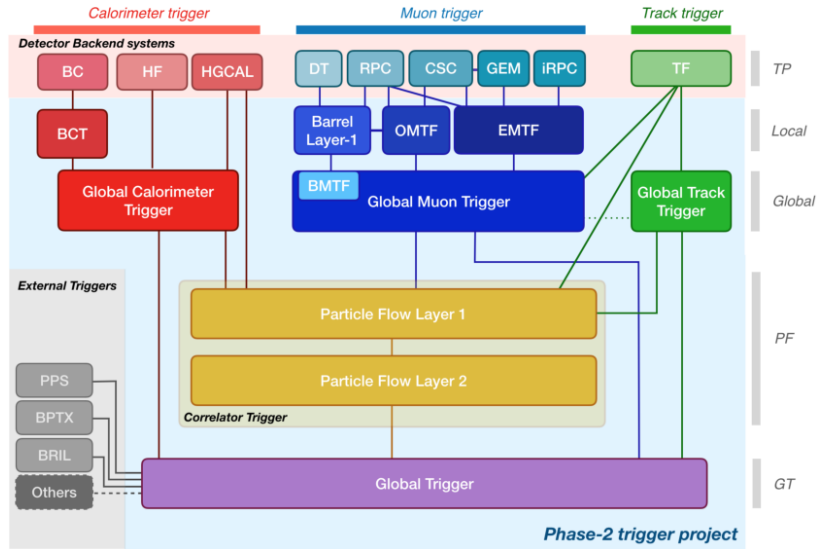


Figure 3.15: Designed trigger architecture of the HL-LHC. The addition of the track primitives allows the computation of more advanced reconstruction algorithms at the L1 level [13].

### 3.2.7.2 High Level Trigger

The HLT receives the full precision detector data for events passing the L1 trigger, and is designed to reduce the final event rate to approximately 100 Hz, five orders of magnitude less than the LHC bunch crossing rate. Information from the tracker allows the HLT algorithms to reconstruct a more complete picture of an event, as tracker information can be matched to both calorimeter hits and muon tracks to provide more detail to reconstructed physics objects. As with the L1 trigger, the HLT processes data through a series of trigger paths, which sequentially reconstruct and filter physics objects. In order to optimize computation time, the HLT uses L1 trigger seed to inform which trigger paths to use, and structures the paths in order of increasing complexity. For example, electrons are first created using only calorimeter data, then matched using coarse hits in the tracker, before being reconstructed using full tracker information. Events passing the HLT are then recorded permanently for offline reconstruction and analysis.

### 3.2.8 Event Reconstruction

Events that pass the HLT then undergo a complete event reconstruction, where data from all sub-detectors is combined to identify each physics object created in a collision. This section provides an description of the relevant objects for this dissertation, namely muons, electrons, and photons, as well as a brief description of the particle flow (PF) algorithm used for global event reconstruction.

#### 3.2.8.1 Tracks and Calorimeter Clusters

Raw detector information taken from the inner tracker and calorimeter are used to create tracks and clusters, which are the building blocks used to create a global event reconstruction. Tracks are built using a Kalman Filter algorithm to fit particle trajectories to hits in the pixel and strip detectors. This process begins with a track seed which is built from hits in the pixel detector compatible with a charged particle track. The initial seed track is propagated outward to collect nearby hits in successive layers of the tracker. Once the seed and hits are collected, the track is iteratively fit to determine the final properties of the charged particle, namely the origin,  $p_T$ , and direction. Various quality cuts are applied based on the number of hits in order to reject fake or misidentified tracks.

Clusters are seeded from individual cells in the calorimeters with an energy above a preset threshold. Adjacent cells are added to the cluster if they have an energy above twice the expected noise level to form superclusters. The average noise level per cell in the electromagnetic calorimeter is roughly 40 and 150 MeV in the barrel and endcap respectively, while the noise per tower in the hadronic calorimeter is around 200 MeV [27]. Lastly, various algorithms calculate the substructure of these topological clusters to separate contributions from individual sources into smaller clusters.

### 3.2.8.2 Muon Reconstruction

Muon reconstruction relies on tracks reconstructed in the inner tracker (tracker tracks) and tracks reconstructed in the muon systems. There are three categories of muon objects based on the method used to reconstruct tracks.

*Standalone-muon tracks* utilize a Kalman-filter algorithm to construct tracks using only information from the muon system. Tracks seeds are formed from CSC or DT track segments and propagated to nearby hits in the muon chambers.

*Global muon tracks* begin with a standalone track, which is propagated to the silicon tracker and matched to compatible tracker tracks. Two tracks are matched if the standalone track and tracker track can be propagated to a common surface. The track is then refit using a Kalman filter by combining the information from the tracker and standalone track.

*Tracker muon tracks* recapture muons in detector gaps and lower  $p_T$  muons that leave hits in the muon chambers but do not fully penetrate the muon system. In these cases, it is common for a muon to leave a segment of hits in consecutive DT/CSC layers that are compatible with a track but not produce a standalone track. Tracker muons are formed by propagating all tracker tracks with  $p_T > 0.5$  GeV and  $p > 2.5$  GeV into the muon chambers, and matching to nearby muon segments.

This reconstruction has an efficiency of 99% for muons produced within the geometric acceptance of the muon system [8]. Muon objects are then fed into the PF algorithm, which performs selection criteria based on the quality of the track. As the purity of each track varies based on type (e.g. hadrons that "punch through" the HCAL are more probable to be reconstructed as track muon tracks), the cuts vary for each category.

### 3.2.8.3 Electron and Photon Reconstruction

In theory, electrons should leave a smoothly curving track in the silicon tracker and deposit nearly all of their energy within a few crystals in the ECAL. However in practice, electrons

frequently interact with the material in the tracker, which induces electromagnetic showers before the particle can reach the calorimeter, resulting in tracks which can have sudden changes in curvature and ECAL clusters that are smeared in  $\phi$ .

The  $e/\gamma$  reconstruction algorithm accounts for these factors when track fitting and forming clusters for electrons. Electron track seeds are formed when the momentum of a track and the energy of an associated ECAL cluster are compatible with unity [27]. These tracks are refit using a Gaussian Sum Filter (GSF), which uses a sum of gaussian distributions to approximate the probability density function for energy loss due to bremsstrahlung [28].

Bremsstrahlung photons are emitted tangent to the trajectory of the electron, which bends in  $\phi$ . To ensure this energy is accounted for in the reconstruction, clusters located tangent to the GSF track are associated to the track and supercluster. Additionally, the total cluster energy is calibrated as a function of energy and  $\eta$  to account for energy loss. Photons, which are seeded by ECAL clusters with no linked GSF track, can undergo the same process of pair production to induce electromagnetic showers. As such, photon candidate clusters are subject to the same energy calibration.

Several cuts are applied to the candidate particles to reject background from hadronic processes. Electrons and photons are expected to have a low ratio of linked HCAL cluster energy to their ECAL cluster energy. Electron tracks have several variables that are fed to a boosted decision tree, which decides whether or not to accept an electron candidate. All tracks, GSR tracks, clusters, and superclusters associated with reconstructed electrons or photons are passed to the PF algorithm.

#### 3.2.8.4 Particle Flow

Particle flow (PF) is a global reconstruction algorithm that takes advantage of the unique signatures of various physics objects as they pass through each detector. It takes information passed from the muon, electron, and photon reconstruction as well as the remaining tracks

and clusters as input to form "pf blocks" in a process known as linking, which topologically associates objects from one or more detector. The particle flow algorithm then takes these blocks and reconstructs the individual particles. In order, the algorithm reconstructs muons, electrons and isolated photons, charged hadrons, and neutral particles. After each step the corresponding tracks and clusters are removed from the pf blocks to prevent double counting. Once all objects are reconstructed, a final post processing step is done to further reduce misreconstructed particles. The PF candidates are used to reconstruct higher level objects such as hadronized quarks and gluons, decay products from  $\tau$  mesons, or  $b$ -quark decays, and calculate the imbalance of transverse momentum created from particles that are invisible to the detector (called missing  $E_T$ , or MET).

## CHAPTER 4

# Real Time Muon Reconstruction at the Compact Muon Solenoid

### 4.1 Introduction

Section 3.2.7.1 provides an overview of the L1 trigger and its importance to the CMS trigger system. This section will detail the design and performance of a Kalman Filter algorithm used in the L1 trigger to identify muon tracks in the barrel region ( $|\eta| < 0.83$ ) of the CMS detector. This algorithm, known as the Kalman Barrel Muon Track Finder (KBMTF), was fully implemented for 2018 data taking and received improvements for continued use in Run-3.

The L1 barrel muon trigger receives inputs from the TwinMux system, which creates trigger primitives by combining information from the DT and RPC detectors to determine the position, trajectory, and timing of hits from incident muons at each station [29]. These hits, referred to as "stubs", are fed to the L1 muon trigger electrons where they are used to reconstruct muon tracks. The previous track finding algorithm, known as the Phase-I Barrel Muon Track Finder (BMTF), used a maximum of two stubs to reconstruct muon trajectories and was designed under the assumption that muons originate only from the beam line. As a part of upgrading the L1 Trigger, the KBMTF algorithm was developed to utilize stubs from all four muon stations as well as reconstruct displaced muon tracks resulting from decays of exotic long lived particles.

## 4.2 The Kalman Filter Algorithm

A Kalman Filter is a tracking algorithm that performs a recursive, iterative chi-square-like fit. Qualitatively, it propagates a system from its current state to the next and combines the predicted value with measurements to "update" the state of the system. This updated system is then iteratively propagated and updated with new measured values. This section focuses on a discrete linear Kalman Filter, which is applicable when a system can be described with a vector of variables whose evolution can be modeled with a linear transformation plus random uncertainties [30].

Abstractly, the state of a system at a given step  $n - 1$  can be described by a vector labeled  $x_{n-1}$  with covariance matrix  $P_{n-1}$ . Let the matrix  $F_n$  represent the linear transformation that propagates  $x_{n-1}$  to the next state  $x_n$ , and the matrix  $Q_n$  be the covariance matrix due to additional uncertainty. The predicted state of the system at step  $n$  can be given by

$$x_n = F_n x_{n-1} \quad \text{and} \quad P_n = F_n P_{n-1} F_n^T + Q_n \quad (4.1)$$

where  $F_n P_{n-1} F_n^T$  represents the propagation of the initial covariance matrix.

Now define a set of measurements taken at state  $n$  as  $z_n$  with covariance matrix  $R_n$ . The measured variables are not restricted to the same set of variables defining  $x_n$  as long as there exist a "change of basis" matrix  $H$  that relates the sets. It should be noted that mathematically  $H$  is not a strict change of basis matrix, as the measured values can have smaller dimensionality than the propagated ones. The predicted state and covariance matrix of the system written in the same variables as the measured quantities are defined as

$$\mu_n = H x_n \quad \text{and} \quad \Sigma_n = H P_n H^T \quad (4.2)$$

Updating the system relies on a matrix known as the Kalman Gain, which acts as a weight based on  $\Sigma_n$  and  $R_n$  and determines if the updated system should skew more towards

the measured or predicted values. The Kalman gain is defined as

$$K := \Sigma_n (\Sigma_n + R_n)^{-1} \quad (4.3)$$

which is then used to calculate the updated system as follows

$$\mu'_n = \mu_n + K(z_n - \mu_n) \quad \text{and} \quad \Sigma'_n = \Sigma_n - K\Sigma_n \quad (4.4)$$

The term  $z_n - \mu_n$  is frequently referred to as the residual of the prediction and measured value. A Kalman gain equal to the identity  $I$  would set the updated coordinates to the measured values, while a Kalman gain of 0 would effectively ignore the measured values. Finally, we substitute  $x_n$  and  $P_n$  into equation 4.4 using equation 4.2 and simplify to give

$$x'_n = x_n + K'(z_n - Hx_n) \quad \text{and} \quad P'_n = P_n - K'HP_n \quad (4.5)$$

where the Kalman Gain  $K$  has been redefined to

$$K' = P_n H^T (H P_n H^T + R_n)^{-1} \quad (4.6)$$

The system  $x'_n$  and  $P'_n$  can now be propagated to step  $n + 1$  where the Kalman Algorithm can be iterated.

### 4.3 The Kalman Barrel Muon Track Finder

A rough outline KBMTF algorithm for track finding is as follows:

1. A track seed is chosen from a stub in the muon station, from which a preliminary track is built. This seed cannot be chosen from the innermost muon station.
2. The track is propagated inward to the next station and matched to the closest stub.

If there is a matching stub, update the track with the stub information. Repeat until the track is at the innermost station.

3. The track is propagated from the innermost station to the beamline. The track properties at this point are stored as the "vertex unconstrained" measurement. These properties include the  $p_T$ ,  $\phi$ ,  $\eta$ , and  $d_{xy}$ , which is defined as the closest distance from the propagated track to the beamline.
4. The vertex propagated track is updated with the constraint that the track originated from the beamline, and the track properties are stored as the "vertex constrained" measurement.

Muon track finding begins at the outer stations in order to get both the vertex unconstrained measurement and the vertex constrained measurement with only one iteration of the KBMTF algorithm. Starting from the inner station and propagating outward would require an additional propagation back inward in order to get the vertex constrained measurement, which would cause the algorithmic latency to exceed timing restrictions. The outer stations are also the lowest occupancy, meaning stubs are less likely to be from background. Tracks are then overlap cleaned, which ensures that stubs are not shared among multiple tracks, and cut and selected based on various goodness of fit criteria. A diagram showing the KBMTF propagation and update procedure can be shown in figure 4.1.

#### 4.3.1 Muon Trajectory Propagation

In order to implement a Kalman Filter, the propagation of muon tracks between stations must be expressed as a linear function of the track variables. From equation 3.6, a charged particle will travel in a circular orbit in the  $\hat{r} - \hat{\phi}$  plane. The high center of mass energy of the LHC results in highly energetic particles, whose trajectories have radii substantially larger than the size of the CMS detector. The large radius of curvature allows us to approximate these trajectories as parabolas. Assume a Cartesian coordinate system with the origin placed

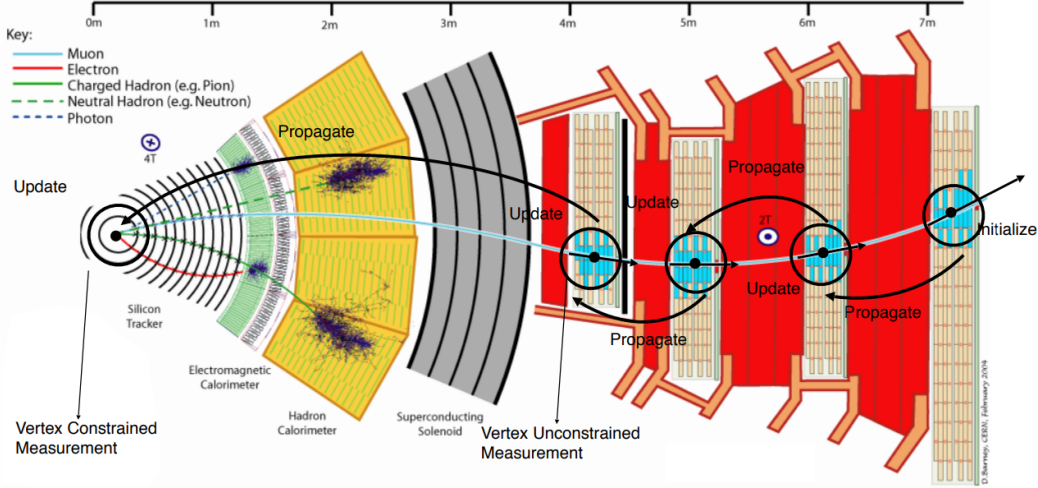


Figure 4.1: The iterative process of propagation and updating a muon track through the KBMTF algorithm. The track properties at the innermost station are stored in order to trigger on muons not originating from the beamline [14].

along a particle's trajectory that has radius  $R$ . This trajectory can then be approximated as

$$y(x) = \frac{x^2}{2R} + bx \quad (4.7)$$

where  $b$  is a coefficient depending on the orientation of the coordinate system. If the initial trajectory is defined as  $\phi_{b,0}$ , taking the derivative and evaluating at the origin yields

$$y'(0) = \tan(\phi_{b,0}) = b \quad (4.8)$$

The curvature  $k = q/p_T$ , where the muon charge  $q = \pm 1$ , is the preferred variable to work with when propagating the trajectory of a muon, as the propagation is linear in  $k$ . Substituting values from equations 3.6 and 4.8 into equation 4.7 yields

$$y(x) = akx^2 + \tan(\phi_{b,0})x \quad (4.9)$$

where  $a = \frac{0.3B}{2}$ . Muon hits, or "stubs", provide information on the position  $\phi$  and bending angle  $\phi_b$ . Let the radius of two sequential muon stations be  $r_1$  and  $r_2$ , with the outer radius given by  $r_2$  and  $\Delta r = r_2 - r_1$ . Assuming a muon has curvature  $k$  at the outer station and ignoring energy loss, equation 4.9 can be used to propagate stubs from the outer station towards the inner station.

$$y(-\Delta r) = (a\Delta r^2) k - \Delta r \tan(\phi_{b,0}) \quad (4.10)$$

$$y'(-\Delta r) = -(2a\Delta r) k + \tan(\phi_{b,0}) \quad (4.11)$$

Converting these to the quantities to angles measured by the detector yields

$$\tan(\Delta\phi) = \frac{y(-\Delta r)}{r_1} \quad (4.12)$$

$$\phi_b = \Delta\phi + \tan^{-1}[y'(-\Delta r)] \quad (4.13)$$

The  $\Delta\phi$  term is added to equation 4.13 because the bending angle at each station is measured relative to an axis system oriented towards the center of the detector. Due to the large radius of curvature of the muon trajectories, the small angle approximation  $\tan(x) \sim \tan^{-1}(x) \sim x$  can be applied, giving the equations

$$\Delta\phi = \frac{a\Delta r^2}{r_1} k - \frac{\Delta r}{r_1} \phi_{b,0} \quad (4.14)$$

$$\phi_b = a\Delta r \left( \frac{\Delta r}{r_1} - 2 \right) k + \left( \frac{r_2}{r_1} \right) \phi_{b,0} \quad (4.15)$$

A diagram showing this propagation can be seen in figure 4.2.

Equations 4.12-4.13 show that the track propagation fits the criteria for a discrete linear Kalman Filter discussed in section 4.2. The matrices for propagation can now be constructed

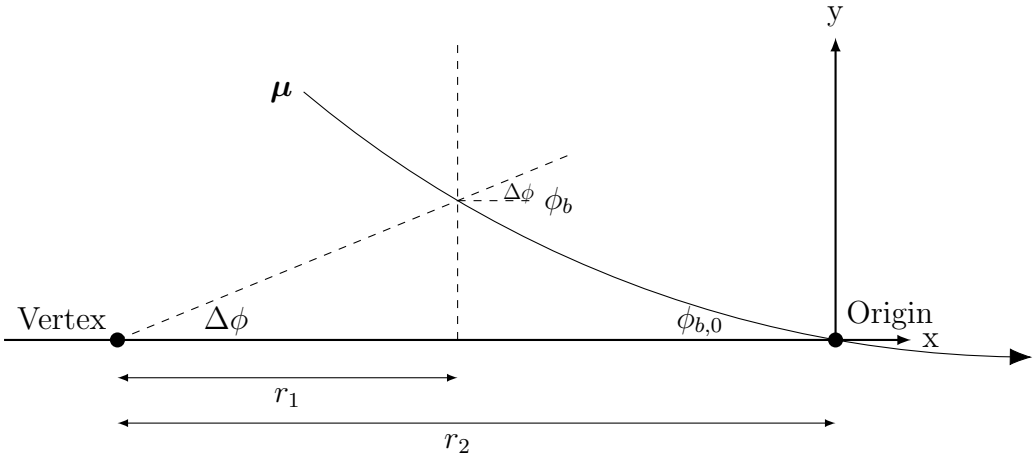


Figure 4.2: Diagram showing a muon trajectory between two stations with the origin set at the outer station. The x-axis is oriented using the detector vertex and the outer station.

as follows. The transfer matrix  $F_n$  from equation 4.1 can be expressed as

$$x_n = \begin{pmatrix} k \\ \phi \\ \phi_b \end{pmatrix}_n = \begin{pmatrix} 1 & 0 & 0 \\ \alpha_n & 1 & -\frac{\Delta r}{r_n} \\ \beta_n & 0 & \frac{r_{n-1}}{r_n} \end{pmatrix} \begin{pmatrix} k \\ \phi \\ \phi_b \end{pmatrix}_{n-1} = F_n x_{n-1} \quad (4.16)$$

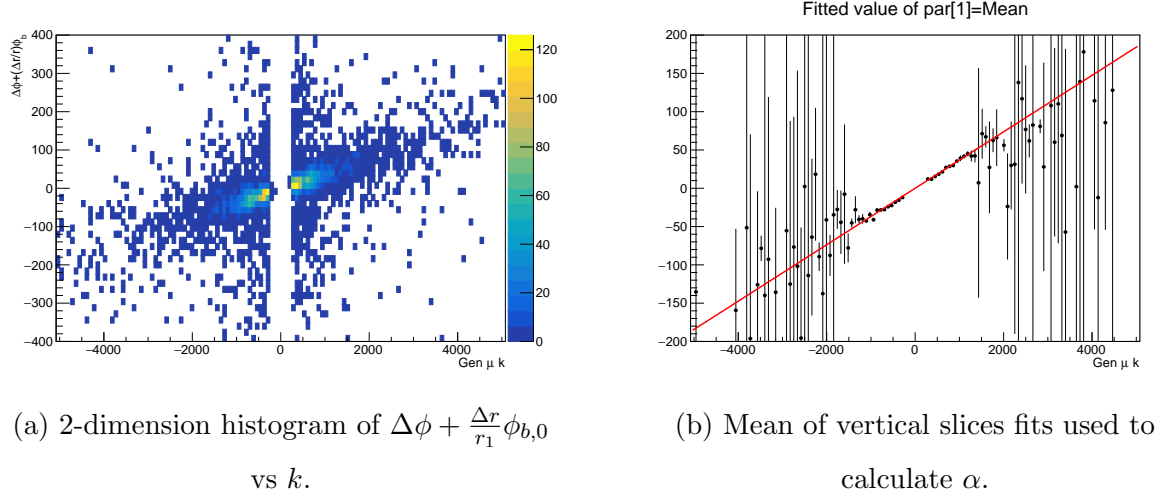
where the coefficients

$$\alpha_n = a \frac{\Delta r^2}{r_n} \quad \text{and} \quad \beta_n = a \Delta r \left( \frac{\Delta r}{r_n} - 2 \right) \quad (4.17)$$

with  $r_{n-1}$  being the radius of the previous (outer) muon station and  $r_n$  the radius of the sequential (inner) muon station.

While the radii of the muon stations are determined by detector geometry, the constants  $\alpha_n$  and  $\beta_n$  are measured using single muon monte-carlo samples where stubs are matched to the incident muons using generator level information. To determine  $\alpha_n$ , stubs in stations  $n$  and  $n - 1$  are first associated if they resulted from the same incident muon. For matching stubs, the quantity  $\Delta\phi + \frac{\Delta r}{r_1}\phi_{b,0}$  is plotted versus the muon  $k$  in a 2-dimensional histogram.

Slices along the y-axis are fit using a Gaussian distribution, and the mean value for each slice is used to calculate a linear fit as a function of  $k$ .  $\beta_n$  is calculated similarly by plotting  $\phi_b - (r_{n-1}/r_n) \phi_{b,0}$  vs  $k$ . This process can be seen in figure 4.3.



(a) 2-dimension histogram of  $\Delta\phi + \frac{\Delta r}{r_1} \phi_{b,0}$  vs  $k$ .  
(b) Mean of vertical slices fits used to calculate  $\alpha$ .

Figure 4.3: Calculation of phi propagation coefficients. Units are converted to their digitized form used in firmware calculations.

### 4.3.2 Covariant Matrices and the Kalman Gain

There are two sources of uncertainty that affect the covariance matrices. The first is multiple coulomb scattering, which occurs when muons scatter elastically with material in the detector. This can be thought of as a small deflection in momentum that alters the trajectory the muon. Lower momentum muons will be deflected at greater angles, so this uncertainty is proportional to  $k$ . Additionally, the probability for multiple scattering is proportional to the amount of material traversed by the muon, so this uncertainty must be calculated for each step in propagation. This is an uncertainty resulting from the propagation, and therefore plays the role of  $Q_n$  from equation 4.1. The second source is from the intrinsic detector resolution, which is a fixed value for each detector. However, the angular resolution is dependent on the radial distance from the center of the detector, so these must be calculated for each

station as well. Since this is an uncertainty on the measurements, the resolution plays the role of  $R_n$  in equation 4.3. The total uncertainty resulting from both of these factors is given by

$$\sigma(k) = \sqrt{\sigma_{ms}^2 k^2 + \sigma_{res}^2} \quad (4.18)$$

The coefficients can be calculated by using the Gaussian slice fits described when deriving  $\alpha$  and  $\beta$ . For each propagation, the sigma of the Gaussian fits is plotted versus  $k$  and fit to the form in equation 4.18. This fitting process for  $\phi$  propagation coefficients is shown in figure 4.4, and is functionally the same for  $\phi_b$ .

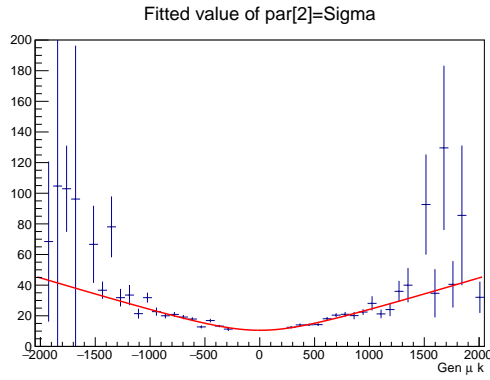


Figure 4.4:  $\sigma$  of vertical slice fits of the 2-dimensional histogram in figure 4.3a used to calculate uncertainty coefficients.

Each stub has a measured value representing the "quality" of the hits, with higher values representing a more precise reconstruction of the bending angle. For this reason, the  $\phi_b$  position resolutions are calculated separately for high and low quality stubs, as the uncertainty can differ by over a factor of 10 between the two.

Since the muon detectors only measure  $\phi$  and  $\phi_b$ , the matrix  $H$  described in equation 4.2 must be a  $2 \times 3$  matrix that takes the form

$$H = \begin{pmatrix} 0 & 1 & 0 \\ 0 & 0 & 1 \end{pmatrix} \quad (4.19)$$

From this, the Kalman Gain  $K'$  defined in equation 4.6 must be a 3x2 matrix with indices  $K_{ij}$ , and the update step can be explicitly written as

$$\begin{aligned} k_n^{\text{upd}} &= k_{n-1} + K_{00}\Delta\phi + K_{01}\Delta\phi_b \\ \phi_n^{\text{upd}} &= \phi_n^{\text{prop}} + K_{10}\Delta\phi + K_{11}\Delta\phi_b \\ \phi_{b,n}^{\text{upd}} &= \phi_{b,n}^{\text{prop}} + K_{20}\Delta\phi + K_{21}\Delta\phi_b \end{aligned} \quad (4.20)$$

where  $\Delta\phi$  and  $\Delta\phi_b$  are the residuals for  $\phi$  and  $\phi_b$ .

#### 4.3.3 Firmware Implementation of the KBMTF

Two minor approximations are made in order to reduce algorithmic latency and memory usage for firmware implementation. The position resolution of  $\phi$  is substantially smaller than the multiple scattering resolution, so the track  $\phi$  is set automatically to the measured stub  $\phi$ . This is equivalent to fixing  $K_{10} = 1$  and  $K_{11} = 0$  in equation 4.20. Secondly, due to the high uncertainty associated with both the measured and propagated  $\phi_b$ , tracks using three or more stubs set  $K_{i1}$  equal to zero and only update using the residual from  $\phi$ .

Although the Kalman Gain can be exactly calculated exactly given the covariance matrices using equation 4.3, matrix inversion is a resource and latency expensive process for the hardware based trigger. Implementing division into hardware is significantly more resource intensive than multiplication, so the calculation of the determinant for matrix inversions would cause the algorithm to exceed the latency requirements for real time track finding. Instead, the values of  $K_{ij}$  are stored in look-up tables (LUTS) as a function of curvature and the combination of stations that were used to update the track, referred to as the track pattern. For tracks with only two stubs, the LUT contains the exact values of the gain that would have been calculated using equation 4.6. For tracks with more than two stubs, this is an approximation that loses some information from updates at previous stations but produces nearly identical performance.

As outlined in section 4.3.2, the  $\phi_b$  resolution coefficients are different for high and low quality stubs, thus the values for  $K_{ij}$  would have to be provided for every possible combination of high and low quality stubs for each track pattern. This would exponentially increase the number of gains stored on LUTs beyond the memory capacity of the hardware. However, from previous approximations, residuals for  $\phi_b$  are not used for tracks containing three or more stubs, which fixes  $K_{01}$  and  $K_{21}$  at 0 for these track patterns. Only gains for track patterns containing two stubs must account for the quality of the stubs. With four stations, this yields six track patterns with four combinations of stub quality that must be stored in LUTs, which is within the capacity of the current hardware.

The firmware is written using Vivado High Level Synthesis (HLS) which compiles firmware written in C to HDL, optimizing it for a given FPGA and clock frequency [31]. When synthesized in a Virtex 7 690T FPGA with a clock frequency of 160 MHz, the KBMTF algorithm can process a single event in 9 bunch crossings, and is pipelined to allow for continuous processing of events. Table 4.1 shows the resource utilization of the KBMTF compared to the previous BMTF algorithm, which was implemented using an identical FPGA and clock frequency.

Algorithm	LUT	FF	BRAM	DSP
Phase I BMTF	43%	23%	35%	0%
KBMTF	16%	11%	15%	25%

Table 4.1: Comparison of FPGA resource utilization [14]. The KBMTF utilizes DSP cores for arithmetic operations to propagate and update tracks and LUTs for the propagation coefficients and approximate Kalman Gain, while the BMTF uses LUTs to assign momentum.

## 4.4 Performance of the Kalman Barrel Muon Track Finder

The performance of an trigger algorithm is primarily determined by the rate and efficiency. The efficiency is the fraction of signal events that successfully have a track reconstructed

by the algorithm, while the rate is the frequency that the algorithm will trigger. A high efficiency is desirable to ensure any interesting events are stored for future analysis, while a low rate is crucial to reject background events and provide a reasonable bandwidth to store events.

#### 4.4.1 Trigger Efficiencies and Rate

The previous L1 barrel muon trigger (BMTF) functioned by using pairs of stubs to form tracks, then using a LUT to assign track parameters based on the  $\phi$  and  $\phi_b$  of the stubs. This LUT takes only the  $\phi$  and  $\phi_b$  of the two stubs and was calculated with the assumption that the muon originated from the beamspot. In the case of displaced muons, which arise from secondary decays of long lived, beyond standard model particles, the assumption is no longer valid and results in large inefficiencies as the muon becomes more displaced from the beamspot.

The general efficiency of a trigger is defined as the fraction of signal muons that have a matching reconstructed track, and can be expressed abstractly as

$$\epsilon = \frac{N_{\text{signal}}(\text{Passing trigger})}{N_{\text{signal}}} \quad (4.21)$$

For muon triggers, the denominator of signal muons consist of events that have known information about the muons. This can be from generator information in simulated monte-carlo samples, tracker information using cosmic muon data, or probe muons using the tag-and-probe method on data. These signal muons are cut using the known muon information to produce a reasonable sample for track reconstruction. The numerator consists of signal muons with a matching reconstructed track that may have addition cuts on the reconstructed track properties.

Figure 4.5 shows the efficiency versus muon  $d_{xy}$  for three track finding algorithms. The denominator consists of cosmic ray muons passing through the barrel muon detectors with a

$p_T > 20$  GeV. The numerator requires a matching L1 track with reconstructed  $p_T > 10$  GeV. The lower threshold for the L1 track is set to prevent the momentum resolution of the reconstruction algorithms from affecting the efficiency. The first algorithm is the BMTF, which shows inefficiencies due to the  $p_T$  LUTs assuming the muon originated at the beamspot. The second is the prompt KBMTF, which uses the vertex constrained measurement. This also shows inefficiencies due to the vertex constraint, but is better than the BMTF as the vertex constraint isn't applied until the last step of track reconstruction. Lastly, the displaced KBMTF uses the vertex unconstrained measurement and shows substantial improvements compared to both prompt algorithms.

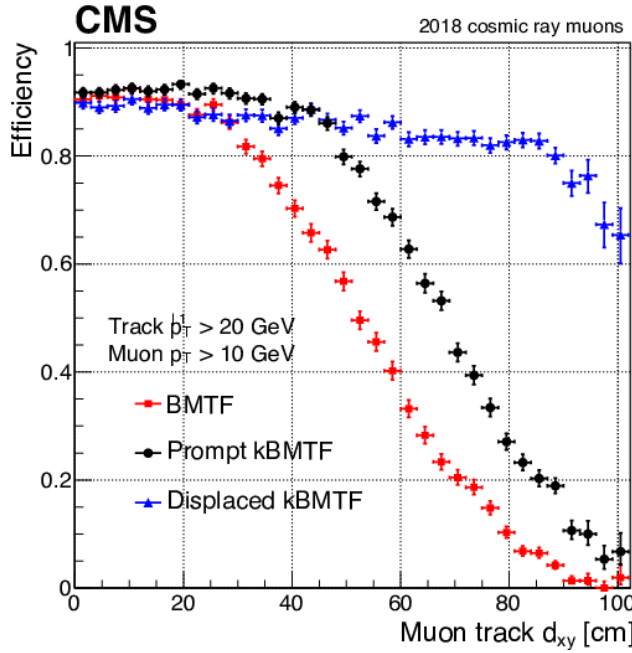


Figure 4.5: Comparison of efficiency vs cosmic track  $d_{xy}$  using cosmic data from the 2018 data taking run. The prompt KBMTF takes the reconstructed  $p_T$  using the vertex constrained measurement, while the displaced KBMTF uses the veretx unconstrained measurement. The displaced KBMTF shows substantial improvements to the previous BMTF [15].

A reconstructed track must have a  $p_T$  above a given threshold to trigger on an event. Thresholds are set to optimize the analysis potential of the data while also minimizing the

additional bandwidth to store events. The rate, which is the frequency at which a trigger decides to store an event, can be calculated as a function of threshold using zero bias data, which is collected by storing random events regardless of trigger acceptance. This creates a representative data set of all  $pp$  collisions, hence the name "zero bias". The rate can be calculated from the zero bias data as follows

$$R = f_{\text{rev}} \times \langle N_{\text{bunches}} \rangle \times \frac{N_{\text{events}}(\text{L1 Track } p_T > \text{Threshold})}{N_{\text{events}}} \quad (4.22)$$

Where  $f_{\text{rev}}$  is the LHC revolution frequency of 11.245 kHz and  $\langle N_{\text{bunches}} \rangle$  is the average number of proton bunches that will collide in one revolution. For 2017 data taking these yield a scale factor of 20984 kHz. Figure 4.6 shows the rate versus threshold for the BMTF, vertex constrained KBMTF, and vertex unconstrained KBMTF.

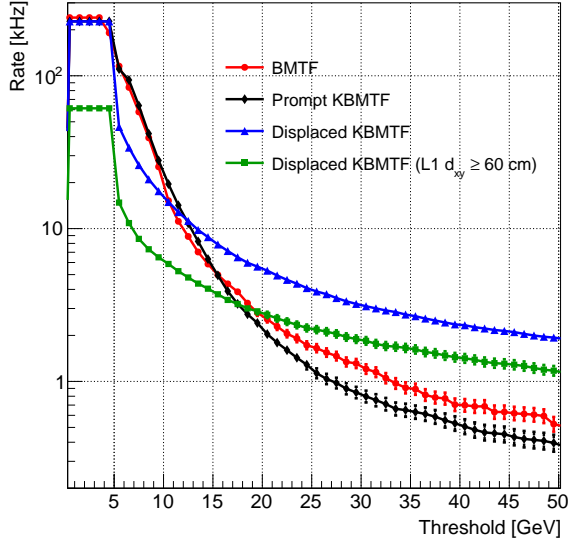


Figure 4.6: Rate comparison calculated using 2017 zero bias data of the Phase I BMTF, vertex constrained (prompt) KBMTF, vertex unconstrained (displaced) KBMTF, and displaced KBMTF for displaced tracks.

#### 4.4.2 Firmware and Emulator Agreement

The performance of the KBMTF is tested using a dedicated C++ software emulator which is integrated into the CMS analysis framework. This emulator follows similar logic to the HLS code, but is not a one-to-one replica. Several modifications are made to the HLS code in order to make it compatible with the synthesis into HDL and pipelining. As such, a test bench is used to ensure that the output of the firmware and emulator are identical. The emulator runs the algorithm over several events and outputs a text file containing information on the input stubs and the reconstructed tracks. This text file is used as input for the test bench, which runs the stub information through the HLS code and compares the properties of the reconstructed tracks to those found in the emulator.

Disagreements between the emulator and firmware are used for a variety of debugging purposes. They frequently point to logic errors in the simplification of the algorithm for HLS synthesis, or in other cases show flaws in the emulator. During Run 2, the disagreements were almost entirely due to differences resulting from fixed point calculations in the firmware compared to floating point calculations in the emulator. These differences have been drastically reduced due to the addition of C++ classes that mimic fixed point calculations in the emulator, which now has a >99.9% agreement to the firmware. Figure 4.6 shows a comparison of the outputs of the firmware and emulator using events from a 2017 Z tag-and-probe sample.

### 4.5 The Phase-2 KBMTF

The modifications to the KBMTF algorithm for the HL-LHC result from increased precision from the input trigger primitives and modifications to the trigger architecture. These changes mainly affect the firmware implementation and do not require conceptual changes to the logic used to propagate and update tracks. The propagation coefficients and Kalman Gain must be recalculated as the number of bits allocated to  $k$ ,  $\phi$ , and  $\phi_b$  change. Additionally,

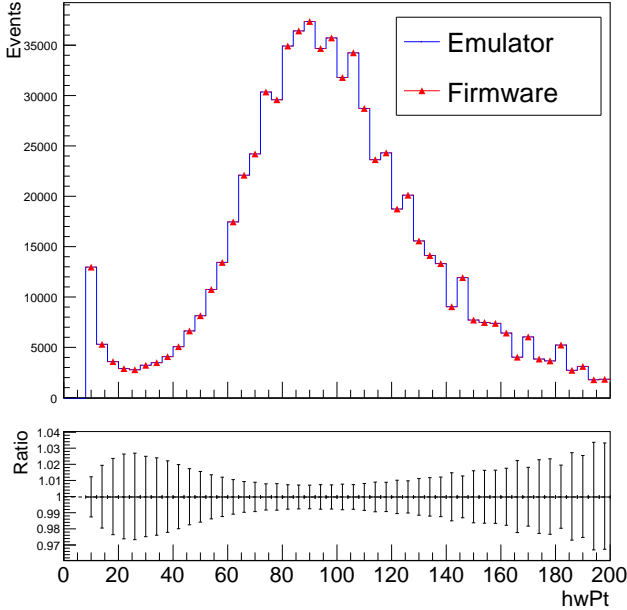


Figure 4.7: Comparison of the track  $p_T$  between the firmware and emulator using data from a 2017 Z tag-and-probe sample. hwPt represents the integer value of  $p_T$  used in hardware. The emulator and firmware output show 100% agreement across 500000 events.

the firmware will receive primitives from the entire barrel muon system simultaneously as opposed to processing each sector in  $\phi$  independently. The firmware will be time-multiplexed with a factor of 18, meaning data from each event will be sent to one of 18 processors running the KBMTF algorithm in parallel. Additionally, the FPGA will be changed to a ZYNQ Ultrascale+ and synthesized at a clock frequency of 200 MHz. Simulations show a resource utilization of 17% LUT, 3% FF, 11% DSP, and 7% BRAM [14].

The KBMTF algorithm performance is robust to the high pileup conditions of the HL-LHC. The efficiencies remain the same as Phase-1, and the rate scales approximately linearly with pileup as expected. Figure 4.8 shows the efficiency versus generated muon  $p_T$ , single muon rates versus threshold, and single muon rates versus pileup for the Phase-2 KBMTF and two proposed track finding algorithms. As discussed in section 3.2.7.1, the HL-LHC track trigger introduces new track primitives that will be used in novel muon triggers. These new

algorithms have higher efficiency and precision for prompt muons due to the momentum resolution of the tracker, but will be unable to trigger on displaced muons as the track primitives do not include displaced tracks.

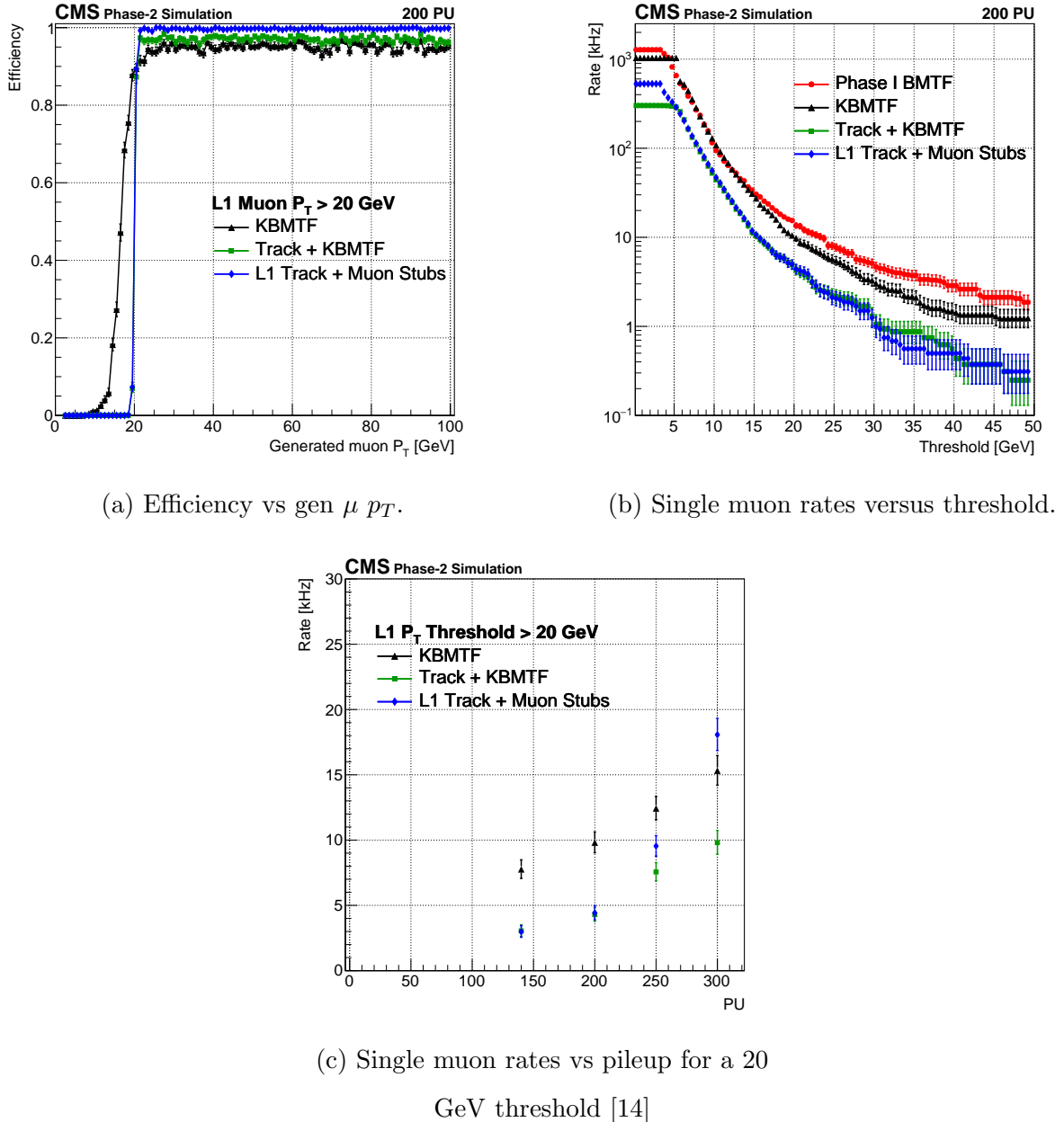


Figure 4.8: Performance of the L1 Barrel Muon algorithms using simulated samples with HL-LHC run conditions. The Track + KBMTF algorithm matches tracks to loose KBMTF muons, while the L1 Track + Muon Stubs algorithm matches tracks to muon stubs.

# CHAPTER 5

## Search for a Long Lived Scalar Boson

### 5.1 Introduction

This chapter describes the search for beyond the standard model (BSM) particles using data taken by the CMS detector from 2016-2018. The following sections outline the choice of datasets and simulated samples, event selection criteria, methods of background estimation and statistical analysis for signal extraction, and results.

### 5.2 Data and Simulated Samples

#### 5.2.1 Data Samples

As discussed in chapter 3, events that pass at least 1 HLT path are stored for future analysis. These events are collected and sorted into datasets based on the number, flavor, and type of physics objects used in the HLT path. It can be noted that these datasets are not disjoint; one event can be sorted into multiple datasets if it satisfies more than a single HLT path. The data is maintained and updated by the Physics Data and Monte Carlo Validation (PdmV) group, which also provides recommendations on optimal usage for physics analysis [32]. This search utilizes the PdmV recommended datasets for Run-2 analyses, referred to as Ultra-Legacy (UL), which has been reprocessed using the most current calibration for detector responses and alignment. Although the characteristic signature of this analysis is two displaced photons, the HLT double photon triggers present in Run-2 are unsuitable for

the phase space of signal photons. Therefore we utilize the leptonic decay of the associated  $Z$  which provides a robust trigger. Since we are interested in  $Z$  decays to either electrons or muons, we use the datasets labeled as SingleMuon or SingleElectron (renamed to EGamma in 2018).

The reprocessed datasets must be cross referenced with the "Golden JSON": a certificate created by the Data Quality Monitoring (DQM) group within CMS by monitoring each sub-detector system in order to veto collisions that occur during sub-optimal conditions. The total integrated luminosity recorded by CMS during Run-2 was  $164 \text{ fb}^{-1}$ ; however, only  $138 \text{ fb}^{-1}$  of that was certified for analysis. The total integrated luminosity and uncertainty per year for collisions recommended by DQM can be seen in table 5.1.

Table 5.1: Table of integrated luminosity per year [16–18].

Year	2016	2017	2018	2016-2018
Luminosity [ $\text{fb}^{-1}$ ]	36.31	41.48	59.83	137.62
Uncertainty [%]	1.2	2.3	2.5	1.6

### 5.2.2 Simulated Samples

Simulated samples use Monte Carlo methods to generate events in several steps, starting from the matrix elements that determine cross sections and hadronization processes and ending with the processing of digitized signals from each subdetector in CMS. These samples are generally created to model specific physics processes such as Drell-Yan, QCD,  $t\bar{t}$ , signal processes, etc. All samples used in this analysis use simulated using parton distribution functions given by NNPDF3.1 [33]. Simulated events are not created one-to-one to match data events; instead they are used to create weighted events that are normalized using the cross section of the simulated process and scaled to match the luminosity of the data. For this analysis we use both simulated background events as well as simulated signal samples.

### 5.2.2.1 Monte Carlo Signal

Standard Model Higgs production through quark-induced and gluon induced  $ZH$  processes are simulated at NNLO for several candidate mass points  $m_\Phi$  and lifetimes  $c\tau$ . The primary hard scattering producing the Higgs Boson and associated  $Z$  boson is simulated using POWHEG BOX v2 [34], while the subsequent decays of the Higgs Boson and showering processes are simulated using Pythia8 [35]. The parameters for Pythia8 simulations were set to TuneCP5, which were the optimal values for agreement with measured data at the time of producing the samples [36]. The simulated signal samples were produced centrally by the Monte Carlo and Interpretation subgroup of CMS.

The Higgs Boson is forced to decay to two long lived scalar bosons ( $\Phi$ ). Each  $\Phi$  has a 50% branching ratio to  $\gamma\gamma$  and a 50% branching ratio to  $d\bar{d}$ , which was set to maximize the number of two photon decays. Additional samples with a 100% branching ratio to  $\gamma\gamma$  were generated to provide better statistics for four photon decays. The  $Z$  is forced to decay to  $\ell\ell$ , which is accounted for when normalizing samples for the limit setting procedure. A complete list of masses, lifetimes, and number of generated events is shown in table 5.2.

Table 5.2: Mass points, lifetimes, and number of simulated  $H \rightarrow \Phi\Phi$  events for the  $2\gamma 2q$  categories. Number of events generated is halved for the  $4\gamma$  categories

$m_\Phi$ [GeV]	$c\tau$ [mm]	Events
15	0, 10, 20, 50, 100, 1000	100000
20, 30, 40, 50, 55	0, 10, 20, 50, 100	50000
	1000	100000

### 5.2.2.2 Signal Lifetime Reweighting

One can interpolate between signal samples using a process known as  $ctau$  reweighting. As each generated event contains two  $\Phi$  with exponentially distributed lifetimes, an event weight

can be applied to generate a sample of arbitrary lifetime. Assume an event generated with mean lifetime  $\tau_0$ , with each  $\Phi$  lifetime given by  $t_1$  and  $t_2$ . To reweight this sample to a new mean lifetime  $\tau_{\text{new}}$ , we apply a weight given by the ratio of poisson probability distributions

$$w(\tau_0, \tau_{\text{new}}, t_1, t_2) = \frac{\mathcal{P}(t_1|\tau_{\text{new}})\mathcal{P}(t_2|\tau_{\text{new}})}{\mathcal{P}(t_1|\tau_0)\mathcal{P}(t_2|\tau_0)} = \left(\frac{\tau_0}{\tau_{\text{new}}}\right)^2 \frac{e^{-\frac{(t_2+t_1)}{\tau_{\text{new}}}}}{e^{-\frac{(t_2+t_1)}{\tau_0}}} \quad (5.1)$$

The  $\Phi$  lifetimes  $t_i$  can be calculated from the generator level information as follows

$$ct = \frac{\beta}{\gamma} \cdot \text{ip}_{3D} = \frac{m|\mathbf{p}|}{E^2} \cdot \text{ip}_{3D} \quad (5.2)$$

Where  $c$  is the speed of light,  $m$ ,  $\mathbf{p}$ , and  $E$  are the mass, 3-momentum, and energy of the  $\Phi$  and the three-dimensional impact parameter  $\text{ip}_{3D}$  is the distance in the lab frame traveled by the  $\Phi$  from the PV before decaying.

Lifetimes are reweighted to 3, 14, 32, 70, and 316 mm to be uniformly distributed between generated signal samples on a logarithmic scale. The signal sample with the nominal lifetime closest to the target lifetime is chosen to be reweighted, excluding the 3 mm sample which is produced using the 10 mm sample.

### 5.2.2.3 Pileup Reweighting

Events passing the HLT generally consist of one interesting hard-scatter occurring at the primary vertex (PV). However, as discussed in chapter 3.2.7, colliding proton bunches often produces secondary collisions along the beamline known as pileup (PU). Particles resulting from PU are generally uninteresting on their own but produce tracks and energy deposits that affect event reconstruction. During Run-2 data taking the average pileup ranged from 27 in 2016 to 37 in 2018. PU distributions in data can be seen in figure 5.1.

Monte Carlo samples account for secondary collisions by generating PU interactions according to a predetermined distribution. However, this distribution does not exactly match

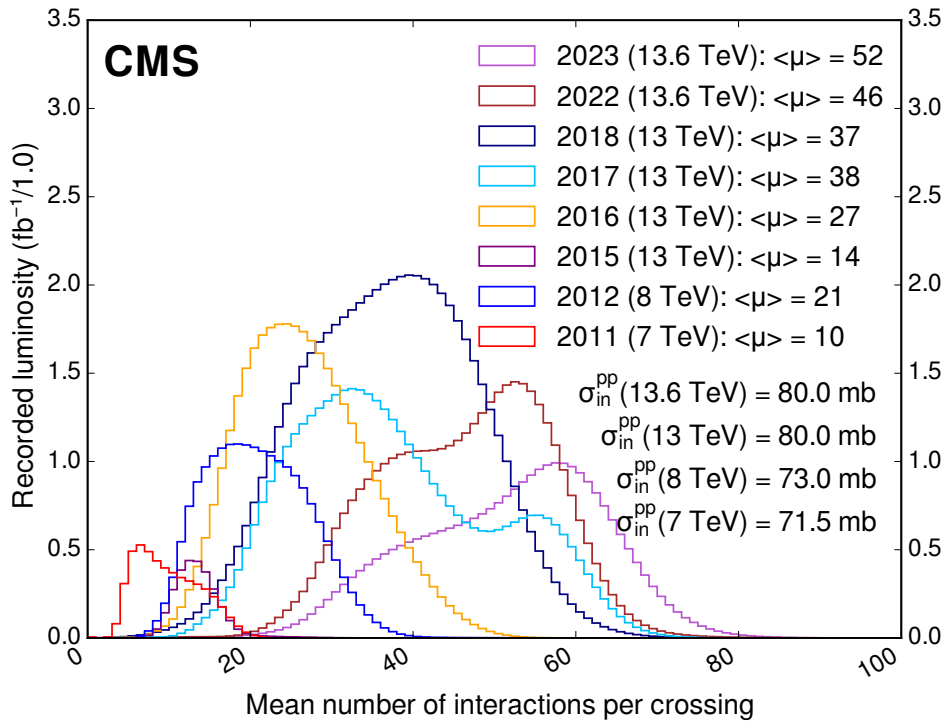


Figure 5.1: Pileup distributions and mean PU from 2011-2023 datataking [1]

what is observed in data. To account for this, we apply a weight to simulated samples as a function of the number of simulated PU interactions by dividing a histogram of data PU distributions by the Monte Carlo PU distribution.

#### 5.2.2.4 Monte Carlo Background

Although this analysis employs a data driven method of background estimation, simulated samples are used to inform on properties of background events and tune cuts to discriminate between signal and background. For this analysis, we use simulated Drell-Yan (DY) to  $\ell\ell$  events with 0, 1 and 2 additional jets, simulated using matrix elements calculated at next-to-next-to leading order (NNLO). Studies were done with inclusive (any number of additional jets) samples but found to have worse agreement and statistical power compared to the jet categorized samples. The cross sections used for normalization were calculated using

the `GenXSecAnalyzer`, a tool provided by CMS to calculate the cross sections for simulated samples [19]. A list of cross sections for each simulated process can be found in table 5.3.

Table 5.3: List of simulated background processes and their cross sections calculated using `GenXSecAnalyzer` [19]

Process	Cross Section [pb]
DY + 0 jets	5090
DY + 1 jet	983.5
DY + 2 jets	353.5

## 5.3 Vertex Reconstruction of Displaced Photon Pairs

### 5.3.1 Diphoton Kinematics

The kinematics of a long lived scalar boson  $\Phi$  decaying to two photons can be precisely described by the following

$$m_\Phi^2 = 2E_1E_2(1 - \cos\theta) \quad (5.3)$$

where the  $m_\Phi$  is the mass of the  $\Phi$ ,  $E_1$  and  $E_2$  are the energies of the two photons, and  $\theta$  is the angle between the two photons. The energy of the two photons is measured by the CMS ECAL, thus  $\theta$  can be calculated as a function of  $m_\Phi$ . Due to the primary vertex, decay vertex, and ECAL clusters being coplanar, this calculation is treated as a 2 dimensional problem. It is a trivial procedure to rotate the system to calculate the vertex, then rotate back to detector coordinates once the decay vertex is calculated. Let the position of the two ECAL clusters be  $\mathbf{r}_1$  and  $\mathbf{r}_2$ . The system can be rotated by an angle

$$\varphi = \arccos \left( \frac{\mathbf{r}_1 \times \mathbf{r}_2}{\|\mathbf{r}_1 \times \mathbf{r}_2\|} \cdot \hat{z} \right) \quad (5.4)$$

around an axis given by

$$\hat{n} = \frac{\mathbf{r}_1 \times \mathbf{r}_2}{\|\mathbf{r}_1 \times \mathbf{r}_2\|} \times \hat{z} \quad (5.5)$$

to determine the decay vertex, then rotated by  $-\varphi$  around the same axis to give the final value.

The geometry of the vertex fit is described in figure 5.2. Assume we have two ECAL clusters and a given value of  $m_\Phi$ . This fixes the value of  $\theta$  from equation 5.3. It will be shown that the locus of points satisfying these constraints corresponds to the arcs of a circle that overlaps the ECAL clusters.

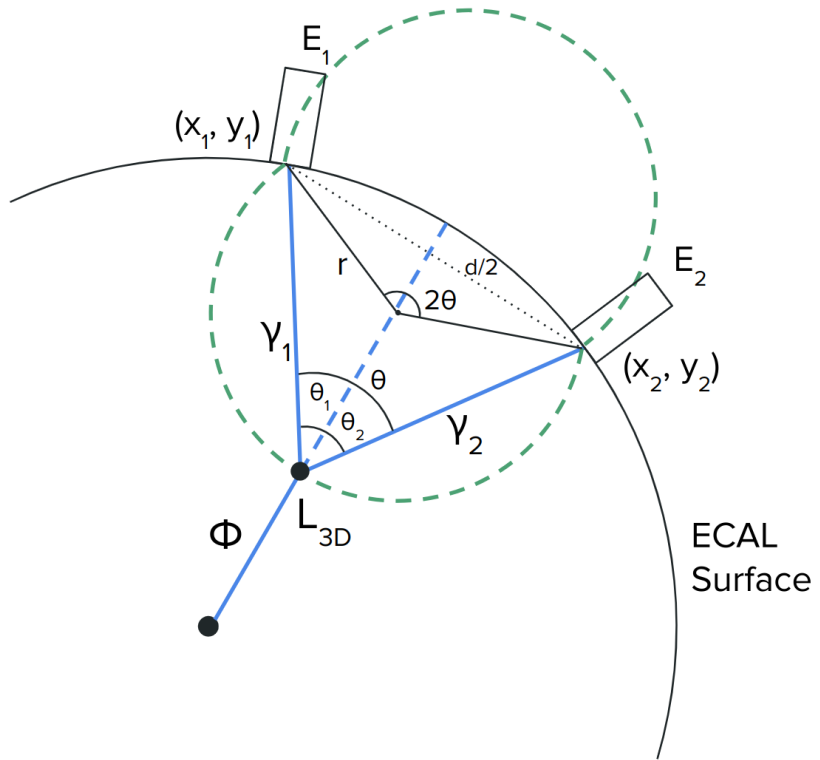


Figure 5.2: Geometrical configuration used to reconstruct the displaced vertex of the di-photon pair

Because three non-collinear points uniquely define a circle,  $\theta$  corresponds to an inscribed angle on a circle which overlaps the decay vertex and the two ECAL clusters located at  $(x_1, y_1)$  and  $(x_2, y_2)$ . The central angle of the arc between the two clusters has measure  $2\theta$

by the inscribed angle theorem. From this, the radius of the circle can be defined by

$$r = \frac{d}{2 \sin \theta} \quad (5.6)$$

where  $d = \sqrt{(x_2 - x_1)^2 + (y_2 - y_1)^2}$  is the distance between the two ECAL clusters. The center of the circle  $(x_0, y_0)$  can be calculated by plugging the two ECAL cluster coordinates into the equation of a circle  $(x - x_0)^2 + (y - y_0)^2 = r^2$ , giving

$$x_0 = \frac{x_1 + x_2}{2} \pm \frac{y_1 - y_2}{q} \cdot \sqrt{r^2 - \frac{q^2}{4}} \quad (5.7)$$

$$y_0 = \frac{y_1 + y_2}{2} \pm \frac{x_2 - x_1}{q} \cdot \sqrt{r^2 - \frac{q^2}{4}} \quad (5.8)$$

$$\text{where } q = \sqrt{(x_1 - x_2)^2 + (y_1 - y_2)^2} \quad (5.9)$$

The two solutions represent circles centered inside and outside of the ECAL. If  $\theta < \pi/2$ , then only the major arcs of the two circle satisfy equation 5.3. Alternatively, if  $\theta > \pi/2$  only the minor arcs are valid solutions. For either solution, an arc from one of two circles will lie outside the ECAL. This arc represents a nonphysical solution and can be discarded, as it would imply the  $\Phi$  both decayed outside of the ECAL and left ECAL clusters. The remaining arc represents the locus of possible decay vertices.

The angle between the two photons can be divided into the deflection of each photon ( $\theta_1$  and  $\theta_2$  respectively), and conservation of momentum requires  $E_1 \sin \theta_1 - E_2 \sin \theta_2 = 0$ . From here, the vertex can be calculated numerically by sampling points along the remaining arc and choosing the coordinates that satisfy this equation.

It should be noted that this method can yield a locus of points that pass behind the beamline resulting in a negative impact parameter. The vertex is still calculated in these cases in order to provide a disjoint region with respect to the signal region that will be used to validate analysis methods and estimate the background yield. A diagram showing a

negative reconstructed vertex is shown in figure 5.3.

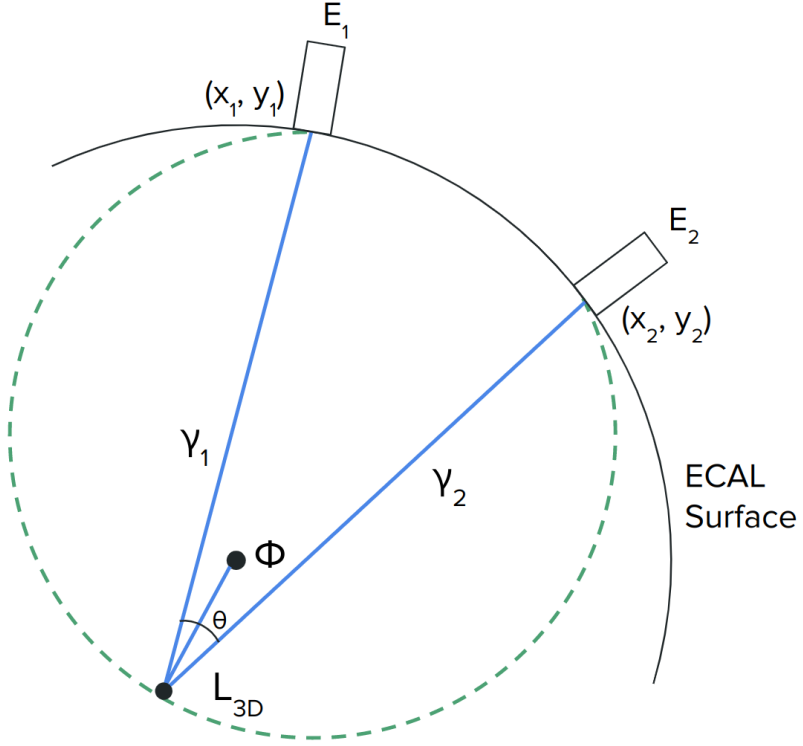


Figure 5.3: Geometrical configuration showing the reconstruction of a negative impact parameter

### 5.3.2 Performance of Diphoton Vertex Calculation

It is evident that since the kinematic fit uses the hypothetical mass of the  $\Phi$ , the fit must be rerun for every hypothetical mass used in this analysis. As a result, the events in the signal region used for each value of  $m_\Phi$  are different. Figure 5.4a shows the reconstructed  $L_{xy}$  behaves as expected as the  $\Phi$  lifetime increases. To demonstrate the resolution of the kinematic fit, we plot the difference between the calculated  $L_{xy}$  and the generator level  $L_{xy}$  as a function of the generator level  $L_{xy}$ , performed using a  $Z \rightarrow \ell\ell$  samples with  $m_\Phi = 30$  GeV, using both the  $c\tau = 100$  mm and 1000 mm samples. These distributions can be seen in figure 5.4b. The vertical slices of this histogram were fit to Gaussian distributions so that

the mean and sigma could be plotted as a function of generator level  $L_{xy}$ . The means shown in figure 5.4c show the differences in calculated and generator  $L_{xy}$  are compatible with zero, and the sigma shown in figure 5.4d show a resolution of  $< 3$  cm, slightly decreasing with generator level  $L_{xy}$ . Both the mean and sigma remain consistent across all ranges of  $m_\Phi$ .

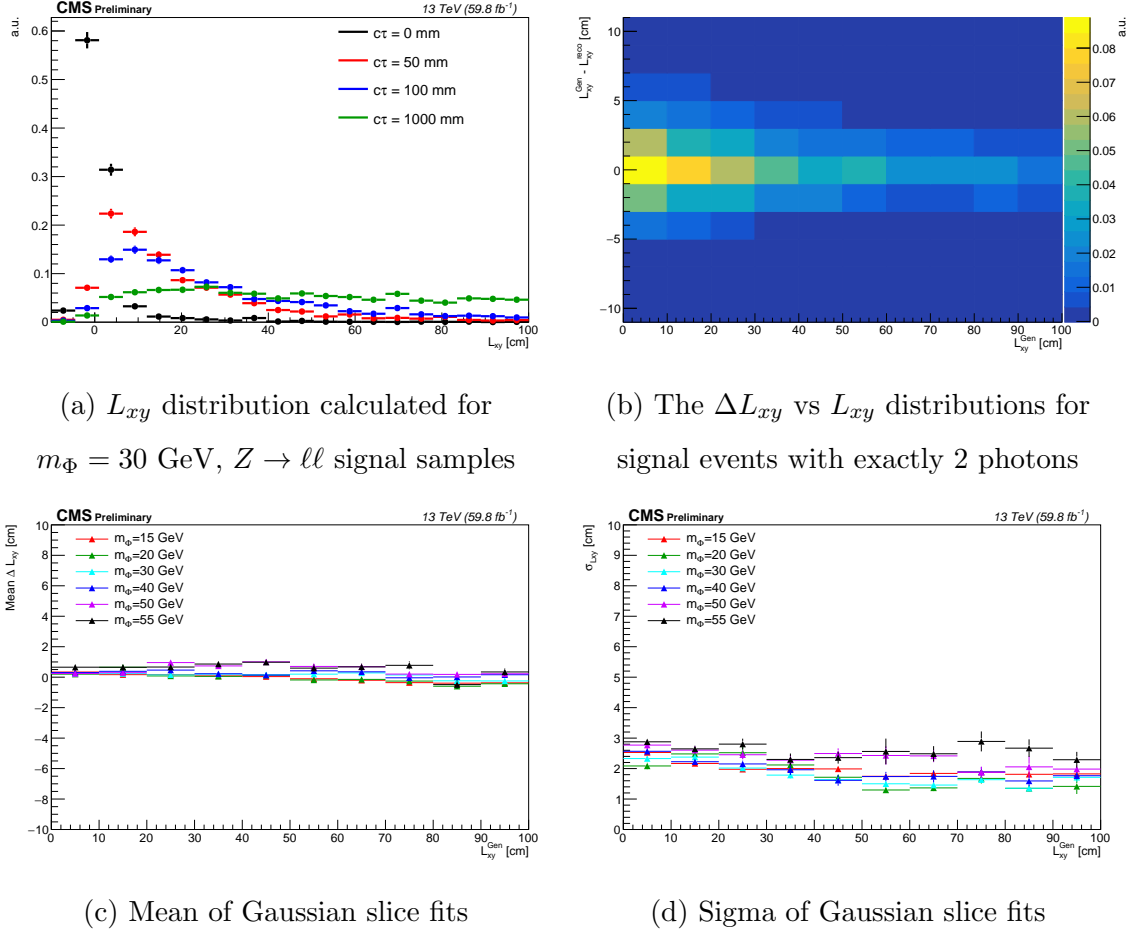


Figure 5.4: Performance of the vertex calculation on signal samples. The fit shows good agreement across all values of generator level  $L_{xy}$  and a resolution of  $< 3$  cm.

It can be shown that the calculated  $L_{xy}$  for an assumed value of  $m_\Phi$  is monotonically decreasing with the prompt invariant diphoton mass  $m_{\gamma\gamma}$ . Assume that two photons have a prompt invariant mass  $m_{\gamma\gamma}$ . Calculating the vertex assuming  $m_\Phi = m_{\gamma\gamma}$  would yield a vertex with  $L_{xy} = 0$  by construction. Calculating the vertex assuming  $m_\Phi > m_{\gamma\gamma}$  would cause the

angle between the two photons given by equation 5.3 to decrease. As the ECAL cluster positions are fixed, this pushes the vertex backwards yielding  $L_{xy} < 0$ . By similar methods, assuming a value of  $m_\Phi < m_{\gamma\gamma}$  yields a vertex with  $L_{xy} > 0$ . The dependence makes the  $L_{xy}$  very sensitive to small changes in the assumed value of  $m_\Phi$ . If the assumed value of  $m_\Phi$  differs from the true mass by 5 GeV, the calculated  $L_{xy}$  can skew upwards or downwards by  $> 20$  cm, depending on the value of the true mass. Figure 5.5 shows the differences in generated and reconstructed  $L_{xy}$ , combining samples for all lifetimes for a given true mass.

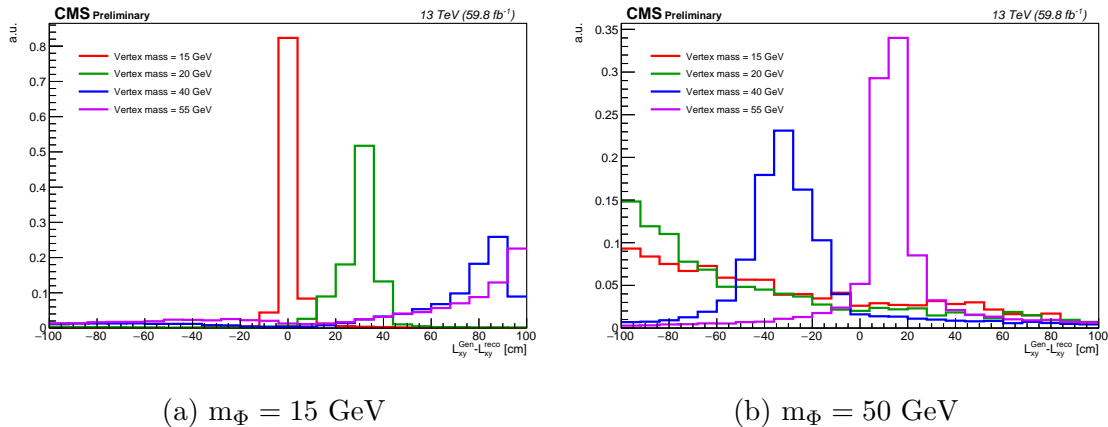


Figure 5.5: The difference between the true and reconstructed vertex grows as the assumed mass departs from the true one. Gen-reconstructed  $L_{xy}$  for a  $Z + H$  samples under several assumed mass points.

This analysis uses the `nanoAODv9` data format - the most compact data tier available for analysis use in CMS. As opposed to lower tier formats which contain detailed collections of classes to store event properties, nanoAOD provides only the most important information for high level physics objects [37]. This information includes several properties of photons but omits the calorimeter cluster position, which is required to calculate the diphoton vertex. To circumvent this, we propagate the photons from the PV to the ECAL using their  $\eta$  and  $\phi$ . The ECAL is approximated using a cylinder with radius  $\rho = 137$  cm and  $z = 324$  cm. These values were obtained using `miniAODv2` samples and are shown in figure 5.6. Diphoton vertices calculated using the propagated coordinates yield a  $L_{xy}$  within 3% of the  $L_{xy}$  calculations

using the exact cluster coordinates, which is well within the intrinsic resolution of the vertex calculation.

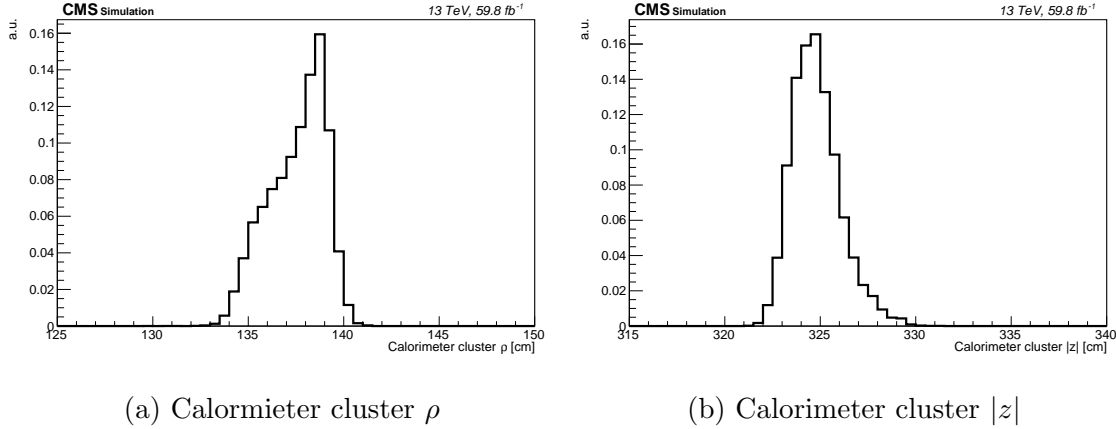


Figure 5.6: The  $\rho$  for barrel photons and  $|z|$  for endcap photons for all reconstructed photons using `miniAODv2` signal samples

## 5.4 Event Selection

The first step in collecting events for the analysis is to select events passing HLT lepton triggers. Events passing these triggers are then chosen based on the presence of two same flavor, opposite charge leptons and two photons. Various quality cuts, referred to as preselection criteria, are applied to these objects to reject background. Lastly, cuts are applied to reject photons from final state radiation (FSR) and low  $p_T$  photons that promoted to displaced  $\Phi$  candidates by the kinematic vertex fit.

### 5.4.1 Triggers

Events are triggered through leptonic decays of the  $Z$  boson produced in association with the SM Higgs Boson. The  $Z$  candidates are selected from dilepton events passing the HLT isolated single lepton triggers. These triggers are the standard lepton triggers recommended

both the EGamma and Muon physics object groups (POGs) in CMS. Double lepton and high  $p_T$  lepton triggers were considered but provide only negligible improvement when applied in addition to the single lepton triggers. Muon events must pass the single muon triggers and are vetoed by the single electron triggers, while electron events must pass single electron triggers and are vetoed by the single muon triggers. A complete list of HLT trigger paths used for each year can be seen in table 5.4.

Table 5.4: HLT trigger paths used for the Run 2 datasets

Year	Single Electron	Single Muon
2018	HLT_Ele32_WPTight_Gsf	HLT_IsoMu24
2017	HLT_Ele32_WPTight_Gsf	HLT_IsoMu27
2016	HLT_Ele27_WPTight_Gsf	HLT_IsoMu24    HLT_IsoTkMu24

## 5.4.2 Preselection Criteria

For both electrons and muons we define a set of tight and loose leptons based on cut based ID set by the EGamma and Muon POGs. To reconstruct a  $Z$  candidate, we require exactly two same flavor opposite charge tight leptons with invariant mass  $70 < m_{\ell\ell} < 110$  GeV and zero additional loose leptons. For photons we require two photons passing a set of preselection criteria, which are subject to additional classification based on cut based ID.

### 5.4.2.1 Particle Flow Isolation

One key application of the particle flow (PF) algorithm is the calculation of a particle's isolation. This quantity measures the  $p_T$  contributions from PF candidates in a fixed  $\Delta R$  cone centered on the original particle. A lower value implies the particle is more isolated (i.e. there are fewer additional particles nearby), and vice versa. Isolation is a key variable to reject particles produced in jets from heavy-flavor hadronic decays or decays of pions and

kaons [27]. A particle's isolation is defined as follows:

$$I_{\text{pf}} = \sum_{\substack{i \in \text{charged} \\ \text{hadrons}}}^{\Delta R} p_T^i + \max \left( 0, \sum_{\substack{i \in \text{neutral} \\ \text{hadrons}}}^{\Delta R} E_T^i + \sum_{\gamma \in \text{photons}}^{\Delta R} E_T^\gamma - \text{PU Corrections} \right) \quad (5.10)$$

Particles created from pileup can create calorimeter deposits within the  $\Delta R$  cone used to calculate isolation. These are unrelated to the physics process for the central particle and can artificially inflate the isolation of a particle. Only charged hadrons originating from the PV are used when calculating the charged hadron isolation, which rejects charged hadrons originating from PU. Neutral particles, however, do not produce tracks, meaning calorimeter deposits from the PV and from pileup are indistinguishable. Because of this, there are additional corrections for the neutral hadron and photon isolation. Two common methods are  $\rho$  corrections, which calculate the average energy density from pileup multiplied by an effective area as a function of  $\eta$ , and  $\delta\beta$  corrections, which calculate the energy from pileup as a function of the charged hadron contribution from PU.

It is also common to refer to a particle's relative isolation, which is defined as

$$I_{\text{rel}} = \frac{I_{\text{pf}}}{p_T} \quad (5.11)$$

#### 5.4.2.2 Muon Criteria

The NanoAOD data format takes reconstructed muons and applies loose cuts before storing the muon properties. These branches contain all muons with  $p_T > 3$  GeV with minimal cuts to reconstruction quality. For the purpose of this analysis, muons are classified as loose if they pass all of the following criteria:

- $p_T > 10$  GeV
- $|\eta| < 2.4$

- $D_{xy} < 0.2$  cm: the transverse distance from the PV to the beamline must be less than 0.2 cm
- $D_z < 0.5$  cm: the longitudinal distance from the PV to the beamline must be less than 0.5 cm
- $I_{\text{rel}}(\Delta R < 0.4, \delta\beta\text{-corrected}) < 0.25$
- Passes loose quality criteria set by the Muon POG
  - Muon must be reconstructed by the PF algorithm
  - Muon must be either a global and/or tracker muon

We define tight muons as a subset of loose muons if they pass the following criteria:

- $I_{\text{rel}}(\Delta R < 0.4, \delta\beta\text{-corrected}) < 0.15$
- Passes tight quality criteria set by the Muon POG
  - Muon must be a global muon
  - The global muon track fit must have  $\chi^2/\text{ndof} < 10$
  - Global track must have at least one hit in a muon chamber
  - Muon track must have segments in at least 2 different muon stations
  - Tracker track  $D_{xy} < 2$  mm
  - Tracker track  $D_z < 5$  mm
  - Tracker track must have at least 1 hit in the pixel detector
  - Tracker track must have hits in more than 5 tracker layers

We also require that one of the two tight muons used to reconstruct the  $Z$  to be the triggering muon, and that the triggering muon have  $p_T > 25$  GeV (28 GeV in 2017) in order to operate above the single muon trigger thresholds.

### 5.4.2.3 Electron Criteria

Analogously to the muon criteria, loose electrons are defined from reconstructed global event description electrons if they pass a set of preselection criteria.

- $p_T > 15 \text{ GeV}$
- $|\eta| < 2.4$
- $|\eta| > 1.57 \text{ } jj \text{ } |\eta| < 1.44$ : rejects photons in the overlap region between the ECAL barrel and endcap
- $D_{xy} < 0.2 \text{ cm}, D_z < 0.2 \text{ cm}$
- Passes cut based ID provided by the EGamma POG at the `veto` working point

Tight electrons are selected from this collection of they pass cut based ID at the `tight` working point. Similar to the muon criteria, we require one of the tight electrons be the triggering electron, and that the triggering electron have  $p_T > 35 \text{ GeV}$ .

The variables used in the cut based ID have different working points for barrel and endcap electrons and are optimized to reject background such as photons in hadronic showers or converted photons. The spread of the calorimeter cluster is measured using  $\sigma_{inj\eta}$ , which is the covariance of the cluster shape measured in a  $5 \times 5$  grid of calorimeter crystals. Clusters from signal electrons are  $\exp(-\sigma_{inj\eta})$ . The  $H/E$  ratio takes the energy of HCAL clusters located behind the ECAL cluster and divides it by the ECAL cluster energy. Electrons in EM showers are expected to have relatively narrower shower shape and deposit less energy in the HCAL than electrons in hadronic showers, so these two variables are strong handles to reject hadronic background. A complete table of variables and cut values can be seen in tables 5.5,5.6.

Table 5.5: Cut based ID selection criteria for barrel electrons in Run-2 [20]

	Veto	Tight
$\sigma_{inj\eta} <$	0.0126	0.0104
$ \Delta\eta_{seed}  <$	0.0463	0.00255
$ \Delta\phi_{In}  <$	0.148	0.022
$H/E <$	$0.05 + 1.16/E + 0.0324\rho/E$	$0.026 + 1.15/E + 0.0324\rho/E$
$I_{rel}(\rho\text{-area corrected}) <$	$0.198 + 0.506/p_T$	$0.0287 + 0.506/p_T$
$ 1/E - 1/p  <$	0.209	0.159
Missing inner hits $\leq$	2	1
Passes conversion veto	True	True

Table 5.6: Cut based ID selection criteria for endcap electrons in Run-2 [20]

	Veto	Tight
$\sigma_{inj\eta} <$	0.0457	0.0353
$ \Delta\eta_{seed}  <$	0.00814	0.00501
$ \Delta\phi_{In}  <$	0.19	0.0236
$H/E <$	$0.05 + 2.54/E + 0.183\rho/E$	$0.0188 + 2.06/E + 0.183\rho/E$
$I_{rel}(\rho\text{-area corrected}) <$	$0.203 + 0.963/p_T$	$0.0445 + 0.963/p_T$
$ 1/E - 1/p  <$	0.132	0.0197
Missing inner hits $\leq$	3	1
Passes conversion veto	True	True

## REFERENCES

- [1] CMS Collaboration. CMS luminosity - public results, 2018. URL: <https://twiki.cern.ch/twiki/bin/view/CMSPublic/LumiPublicResults>.
- [2] CMS Collaboration. The high-luminosity lhc (hl-lhc). URL: <https://voisins.web.cern.ch/en/high-luminosity-lhc-hl-lhc>.
- [3] Tai Sakuma. Cutaway diagrams of CMS detector. 2019. URL: <http://cds.cern.ch/record/2665537>.
- [4] The Tracker Group Of The CMS Collaboration. The cms phase-1 pixel detector upgrade, 2020. URL: <https://arxiv.org/abs/2012.14304>, doi:10.48550/ARXIV.2012.14304.
- [5] S Chatrchyan et al. Alignment of the CMS silicon tracker during commissioning with cosmic rays. *JINST*, 5:T03009, 2010. URL: <https://cds.cern.ch/record/1211825>, arXiv:0910.2505, doi:10.1088/1748-0221/5/03/T03009.
- [6] Badder Marzocchi. Simulation of the cms electromagnetic calorimeter response at the energy and intensity frontier. *Journal of Physics: Conference Series*, 1162:012007, 01 2019. doi:10.1088/1742-6596/1162/1/012007.
- [7] Albert M Sirunyan et al. Calibration of the CMS hadron calorimeters using proton-proton collision data at  $\sqrt{s} = 13$  TeV. *JINST*, 15:P05002, 2020. Replaced with the published version. Added the journal reference and the DOI. All the figures and tables can be found at <http://cms-results.web.cern.ch/cms-results/public-results/publications/PRF-18-001> (CMS Public Pages). URL: <https://cds.cern.ch/record/2691403>, arXiv:1910.00079, doi:10.1088/1748-0221/15/05/P05002.
- [8] A.M. Sirunyan et al. Performance of the CMS muon detector and muon reconstruction with proton-proton collisions at  $\sqrt{s} = 13$  TeV. *JINST*, 13(06):P06015, 2018. Replaced with the published version. Added the journal reference and the DOI. All the figures and tables can be found at <http://cms-results.web.cern.ch/cms-results/public-results/publications/MUO-16-001> (CMS Public Pages). URL: <http://cds.cern.ch/record/2313130>, arXiv:1804.04528, doi:10.1088/1748-0221/13/06/P06015.
- [9] CMS Collaboration. Muon drift tubes. URL: <https://cms.cern/detector/detecting-muons/muon-drift-tubes>.
- [10] Isabelle Helena J De Bruyn. Electronics upgrade for the CMS CSC muon system at the High Luminosity LHC. Technical report, CERN, Geneva, 2019. URL: <http://cds.cern.ch/record/2797803>.

- [11] Priyanka Kumari. Improved-rpc for the cms muon system upgrade for the hl-lhc, 2020. URL: <https://arxiv.org/abs/2005.11396>, doi:10.48550/ARXIV.2005.11396.
- [12] Albert M Sirunyan et al. Performance of the CMS Level-1 trigger in proton-proton collisions at  $\sqrt{s} = 13$  TeV. *JINST*, 15(10):P10017, 2020. Replaced with the published version. Added the journal reference and the DOI. All the figures and tables can be found at <http://cms-results.web.cern.ch/cms-results/public-results/publications/TRG-17-001> (CMS Public Pages). URL: <https://cds.cern.ch/record/2721198>, arXiv: 2006.10165, doi:10.1088/1748-0221/15/10/P10017.
- [13] Benjamin Radburn-smith. Overview of the hl-lhc upgrade for the cms level-1 trigger. page 639, 12 2022. doi:10.22323/1.414.0639.
- [14] The Phase-2 Upgrade of the CMS Level-1 Trigger. Technical report, CERN, Geneva, 2020. Final version. URL: <https://cds.cern.ch/record/2714892>.
- [15] Aram Hayrapetyan et al. Development of the CMS detector for the CERN LHC Run 3. Technical report, CERN, Geneva, 2023. URL: <https://cds.cern.ch/record/2870088>, arXiv:2309.05466.
- [16] Albert M Sirunyan and other. Precision luminosity measurement in proton-proton collisions at  $\sqrt{s} = 13$  TeV in 2015 and 2016 at CMS. *Eur. Phys. J. C*, 81(9):800, 2021. Replaced with the published version. Added the journal reference and the DOI. All the figures and tables can be found at <http://cms-results.web.cern.ch/cms-results/public-results/publications/LUM-17-003> (CMS Public Pages). URL: <https://cds.cern.ch/record/2759951>, arXiv:2104.01927, doi:10.1140/epjc/s10052-021-09538-2.
- [17] CMS luminosity measurement for the 2017 data-taking period at  $\sqrt{s} = 13$  TeV. Technical report, CERN, Geneva, 2018. URL: <https://cds.cern.ch/record/2621960>.
- [18] CMS luminosity measurement for the 2018 data-taking period at  $\sqrt{s} = 13$  TeV. Technical report, CERN, Geneva, 2019. URL: <https://cds.cern.ch/record/2676164>.
- [19] CMS Collaboration. How to compute cross sections with the genxsec analyzer. URL: <https://twiki.cern.ch/twiki/bin/viewauth/CMS/HowToGenXSecAnalyzer>.
- [20] CMS Collaboration. Cut based electron id for run 2. URL: <https://twiki.cern.ch/twiki/bin/view/CMS/CutBasedElectronIdentificationRun2>.
- [21] Oliver Sim Brüning, Paul Collier, P Lebrun, Stephen Myers, Ranko Ostojic, John Poole, and Paul Proudlock. *LHC Design Report*. CERN Yellow Reports: Monographs. CERN, Geneva, 2004. URL: <https://cds.cern.ch/record/782076>, doi: 10.5170/CERN-2004-003-V-1.

- [22] Esma Mobs. The CERN accelerator complex - august 2018. complexe des accélérateurs du CERN - août 2018. Aug 2018. General Photo. URL: <https://cds.cern.ch/record/2636343>.
- [23] The CMS Collaboration. Description and performance of track and primary-vertex reconstruction with the cms tracker. *Journal of Instrumentation*, 9(10):P10009, oct 2014. URL: <https://dx.doi.org/10.1088/1748-0221/9/10/P10009>, doi:10.1088/1748-0221/9/10/P10009.
- [24] R. L. Workman and Others. Review of Particle Physics. *PTEP*, 2022:083C01, 2022. doi:10.1093/ptep/ptac097.
- [25] E. Tournefier. The preshower detector of cms at lhc. *Nuclear Instruments and Methods in Physics Research Section A: Accelerators, Spectrometers, Detectors and Associated Equipment*, 461(1):355–360, 2001. 8th Pisa Meeting on Advanced Detectors. URL: <https://www.sciencedirect.com/science/article/pii/S0168900200012432>, doi:10.1016/S0168-9002(00)01243-2.
- [26] G Baiatian et al. Design, Performance, and Calibration of CMS Hadron-Barrel Calorimeter Wedges. Technical Report 1, CERN, Geneva, 2008. URL: <http://cds.cern.ch/record/1049915>, doi:10.1140/epjc/s10052-008-0573-y.
- [27] A.M. Sirunyan et al. Particle-flow reconstruction and global event description with the cms detector. *Journal of Instrumentation*, 12(10), October 2017. URL: <http://dx.doi.org/10.1088/1748-0221/12/10/P10003>, doi:10.1088/1748-0221/12/10/p10003.
- [28] W Adam, R Frühwirth, A Strandlie, and T Todorov. Reconstruction of electrons with the gaussian-sum filter in the cms tracker at the lhc. *Journal of Physics G: Nuclear and Particle Physics*, 31(9):N9–N20, July 2005. URL: [http://dx.doi.org/10.1088/0954-3899/31/9/n01](http://dx.doi.org/10.1088/0954-3899/31/9/N01), doi:10.1088/0954-3899/31/9/n01.
- [29] A. Triossi, M. Bellato, J.M. Cela Ruiz, J. Ero, C. Fernandez Bedoya, G. Flouris, C. Foudas, L. Guiducci, N. Loukas, A. Navarro Tobar, S. Mallios, G. Masetti, F. Montecassiano, E. Paradas, I. Redondo Fernandez, D. Redondo Ferrero, J. Sastre, P. Sphicas, S. Ventura, and C. Wulz. The cms barrel muon trigger upgrade. *Journal of Instrumentation*, 12(01):C01095, jan 2017. URL: <https://dx.doi.org/10.1088/1748-0221/12/01/C01095>, doi:10.1088/1748-0221/12/01/C01095.
- [30] R. Frühwirth. Application of kalman filtering to track and vertex fitting. *Nuclear Instruments and Methods in Physics Research Section A: Accelerators, Spectrometers, Detectors and Associated Equipment*, 262(2):444–450, 1987. URL: <https://www.sciencedirect.com/science/article/pii/0168900287908874>, doi:10.1016/0168-9002(87)90887-4.

- [31] Michail Bachtis. Upgrade of the CMS Barrel Muon Track Finder for HL-LHC featuring a Kalman Filter algorithm and an ATCA Host Processor with Ultrascale+ FPGAs. Technical report, CERN, Geneva, 2019. URL: <https://cds.cern.ch/record/2648953>, doi:10.22323/1.343.0139.
- [32] CMS Collaboration. Pdmvgroupdescription. URL: <https://twiki.cern.ch/twiki/bin/viewauth/CMS/PdmVGroupDescription>.
- [33] Richard D. Ball, Valerio Bertone, Stefano Carrazza, Luigi Del Debbio, Stefano Forte, Patrick Groth-Merrild, Alberto Guffanti, Nathan P. Hartland, Zahari Kassabov, José I. Latorre, Emanuele R. Nocera, Juan Rojo, Luca Rottoli, Emma Slade, and Maria Ubiali. Parton distributions from high-precision collider data: Nnpdf collaboration. *The European Physical Journal C*, 77(10), October 2017. URL: <http://dx.doi.org/10.1140/epjc/s10052-017-5199-5>, doi:10.1140/epjc/s10052-017-5199-5.
- [34] Simone Alioli, Paolo Nason, Carlo Oleari, and Emanuele Re. A general framework for implementing NLO calculations in shower Monte Carlo programs: the POWHEG BOX. *JHEP*, 06:043, 2010. arXiv:1002.2581, doi:10.1007/JHEP06(2010)043.
- [35] Christian Bierlich, Smita Chakraborty, Nishita Desai, Leif Gellersen, Ilkka Helenius, Philip Ilten, Leif Lönnblad, Stephen Mrenna, Stefan Prestel, Christian T. Preuss, Torbjörn Sjöstrand, Peter Skands, Marius Utheim, and Rob Verheyen. A comprehensive guide to the physics and usage of pythia 8.3, 2022. arXiv:2203.11601.
- [36] A. M. Sirunyan, A. Tumasyan, W. Adam, et al. Extraction and validation of a new set of cms pythia8 tunes from underlying-event measurements. *The European Physical Journal C*, 80(1), Jan 2020. doi:10.1140/epjc/s10052-019-7499-4.
- [37] Marco Peruzzi, Giovanni Petrucciani, Andrea Rizzi, and for the CMS Collaboration. The nanoaod event data format in cms. *Journal of Physics: Conference Series*, 1525(1):012038, apr 2020. URL: <https://dx.doi.org/10.1088/1742-6596/1525/1/012038>, doi:10.1088/1742-6596/1525/1/012038.